Plasmonic Coupling Architectures for Enhanced Photocatalysis

*Dr. Dong Liu, and Prof. Can Xue**

Dr. D. Liu, Prof. C. Xue
School of Materials Science and Engineering, Nanyang Technological University, 50 Nanyang Avenue, 639798, Singapore
E-mail: cxue@ntu.edu.sg

Keywords: Photocatalyst, plasmon coupling, surface plasmon resonance, coupled metal nanostructures, solar energy conversion

Abstract

Plasmonic photocatalysis is a promising approach for solar energy transformation. Comparing with isolated metal nanoparticles, the plasmonic coupling architectures can provide further strengthened local electromagnetic field and boosted light-harvesting capability through optimal control over the composition, spacing and orientation of individual nano-components. As such, when integrated with semiconductor photocatalysts, the coupled metal nanostructures can dramatically promote the exciton generation and separation through plasmonic coupling driven charge/energy transfer towards superior photocatalytic efficiencies. Herein, this review presents the principles of plasmonic coupling effect and summarizes recent progress on the construction of plasmonic coupling architectures and their integration with semiconductors for enhanced photocatalytic reactions. In the end, we elaborate the remaining challenges on the rational design and utilization of plasmon coupling structures, and raised some prospects to inspire new opportunities on the future development of plasmonic coupling structures for efficient and sustainable light-driven reactions.

1. Introduction

Efficiently harnessing solar energy has become a very important strategy to achieve energy and environmental sustainability in recent decades.[1-3] Basically, solar energy could be artificially utilized through the transformations to electric energy, chemical energy and thermal energy. The efficiencies of these paths are ultimately determined by the intrinsic properties of the photoactive materials, including their light-harvesting abilities, charge carrier separation and conductivity, and other specific issues. Focusing on these factors, plasmonic metal nanomaterials have been introduced into solar energy conversion systems in recent years.[4-7] Plasmonic nanostructures could interact with incident photons via the excitation of localized surface plasmon resonance (LSPR) and display strong and unique optical responses. This resonance process enables plasmonic nanostructures to trap the energy of light, concentrate it near the surface, and convert light energy into energetic charge carriers and heat.[8,9] Accordingly, plasmonic metal nanostructures have been widely used in solar cells, electronics, sensors, Raman spectroscopy, phototherapy, and solar-driven reactions.[10-15]

Surface plasmons (SPs) are collective electron oscillations that arise at the metal/dielectric or metal/vacuum interface under electromagnetic irradiation.[16] When the size of metal particle is considerably smaller than the wavelength of incident light, confinement of surface plasmons in the metal particle occurs as localized SPs, which present resonance effect as LSPR if the oscillation frequency coincides with the frequency of incident photons. The intensity and frequency of LSPR highly depend on the metal nanostructures' morphology, size, dispersion, composition and the surrounding dielectric environment.[16-18] Many metal nanostructures have LSPR frequencies overlapping with the solar spectrum.

Under LSPR excitation, electromagnetic (EM) fields near the surface of plasmonic metal nanostructures are greatly enhanced and light absorption could be distinctly boosted near the resonant frequency, which could competently meet the demands of solar-driven reactions.[8,19]

Besides, the intrinsic catalytic activity of metal nanostructures will also contribute to the photocatalysis process. Accordingly, different types of plasmonic metal nanostructures with tunable optical performance have been applied in solar-driven reactions, including Ag and Au nanoparticles (NPs), nanorods (NRs), nanospheres (NSs), and nanocubes (NCs).[20-24] Through creation of energetic charge carriers and broadening of the absorption spectrum, these plasmonic metal nanostructures could effectively promote photocatalytic performance in H_2 production, CO_2 reduction and other photoredox reactions.[25-29]

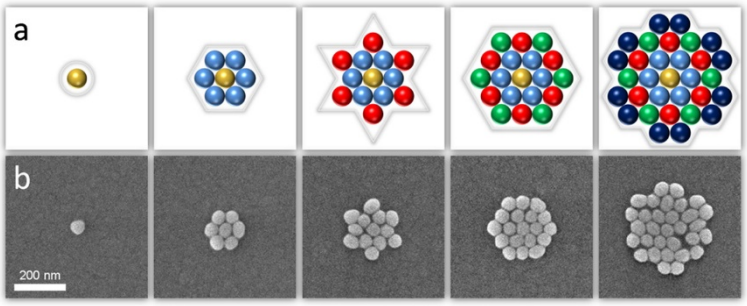

Figure 1. (a) Schematic illustration and (b) the corresponding SEM images of coupled plasmonic Au oligomers. Reproduced with permission.[30] Copyright 2017, American Chemical Society (ACS).

When two or more metal plasmonic NPs approach each other with a distance much smaller than the NP size, their plasmonic resonances will strongly hybridize as plasmonic coupling,[31,32] which strengthens the EM field at the interface and surface of coupled nanostructures. Moreover, the intensity and frequency of the resonance position will alter depending on the surface charge density distribution in the coupled nanostructures.[32] As such, manipulating the configuration of coupled metal nanostructures can tune the EM field and light trapping ability. For example, **Figure 1** displays the schematic and SEM images of Au oligomers of different configurations.[30] In general, comparing with isolated plasmonic metal NPs, coupled nanostructures will present shifted and/or broadened LSPR features.[33] In addition, experimental and theoretical studies have confirmed that multiplied or exponential enhancement of electric field can be induced in the gap region as a “hot spot” between the

coupled nanostructures.[34-36] These hot spots will accelerate energetic charge carrier formation and couple with molecules easily for efficient charge transfer to initiate chemical transformation in the photocatalysis system.[37,38] All these characteristics make plasmonic coupling nanostructures more promising in solar-driven reactions as compared with isolated plasmonic nanoparticles.

Through different chemical synthesis and fabrication methods, various configurations of coupled plasmonic metal nanostructures have been designed and prepared in the forms of dimers, oligomers, core–shell structure, self-assembled chains, nanoarrays, and others.[39-42], One can achieve tunable plasmonic coupling effect by managing the structural configurations to control the LSPR wavelengths and the plasmonic hot spots with strong EM field. The size, distance, orientation and dielectric spacer of these coupled nanostructures could all impact EM field distribution, and thereby could be employed to achieve desirable optical performance.[43-45] Therefore, plasmonic coupling effect could yield significant outcomes in solar-driven reactions upon appropriate design and structural manipulation.

In this review, we will discuss the fundamentals of plasmonic coupling effect, and present an overview on recent advances of plasmonic coupling structures for solar-driven chemical conversion. The review begins with introducing the concept of plasmonic coupling and its impact in photocatalysis, followed by elaboration of the features of plasmonic coupling nanostructures, particularly focusing on the strongly enhanced EM field and consequent phenomena. Then different models of plasmonic coupling are described for guiding the design and manipulation of the coupled nanostructures. The efficacies and advantages of plasmonic coupling in solar-driven reactions are highlighted in the following section based on the points of light absorption, charge kinetics and chemical transformations. In the end, we conclude by providing our perspectives on current studies of plasmonic coupling and comment on prospective directions for the future development of plasmonic coupling architectures.

2. Fundamentals of Plasmonic Coupling

2.1 Plasmonics in Metal Nanostructures

Surface plasmon resonance (SPR) can be defined as the stimulated resonant oscillation of conduction electrons upon external electromagnetic radiation when the frequency of incident photons coincides with the intrinsic oscillation frequency of the surface conduction electrons.[16,46] There are two typical types of SPR, resonance of surface plasmon polariton (SPP) and localized surface plasmon resonance (LSPR).[47] PPs are electromagnetic surface waves propagating across the metal/dielectric or metal/vacuum interface, and have subwavelength-scale confinement, as shown in **Figure 2**a. The excitation of SPPs occurs through the coupling of EM field of incident photons with the electrons on the bulk metal surface. LSPR is the collective coherent oscillation of conduction electrons confined on the metal nanostructure surface (Figure 2b).[48] A restoring Coulombic attraction force arises between electrons and the nucleus when the electron clouds are displaced under the electric field from incident light, leading to the oscillation of electron clouds with respect to the positive nucleus. The resonant oscillation frequency is determined by the intrinsic characteristics of charges in metal nanostructures, such as the density of electrons and the charge distribution.[46]

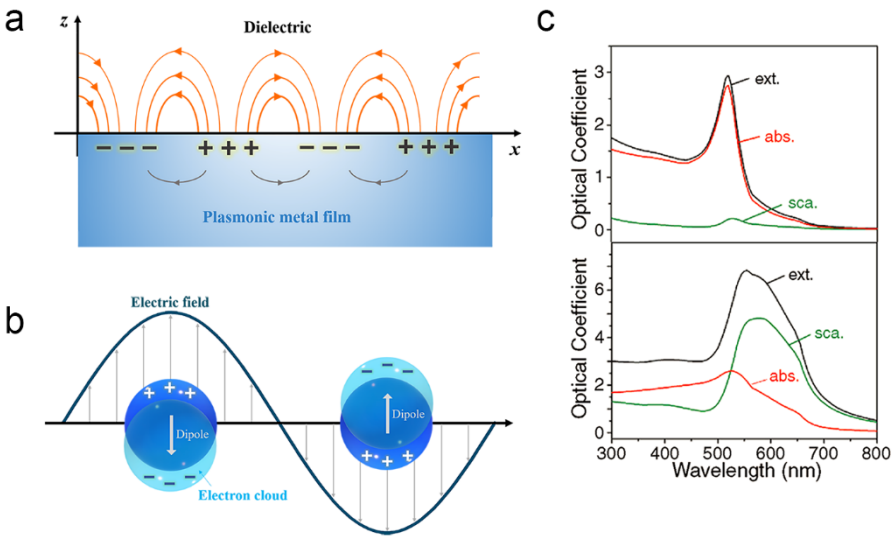

Figure 2. Schematic illustrations of two modes of SPR: a) SPP; b) LSPR. c) Calculated extinction spectra of Au

nanospheres in water with radius of 20 nm (top) and 50 nm (bottom). c) Reproduced with permission.[49] Copyright 2005, Materials Research Society.

The excitation of LSPR can induce near-surface EM field enhancement and maximal light extinction at the resonant frequency.[16] The interaction of nanostructures with the incident photons can be investigated by solving Maxwell's equations with appropriate boundary conditions. For a single spherical nanoparticle with diameter *D*, Mie theory can describe the electrodynamic response with the incident light with wavelength λ under simple quasistatic approximation condition.[6] In this circumstance, the phase of oscillating EM field is regarded as nearly constant in the homogeneous nanosphere with isotropic surrounding medium. The electric field of external plane-wave light is

$$\boldsymbol{E} = \mathrm{E}_0 e^{-i\omega t}\boldsymbol{x} \quad (1)$$

where E_0 is a content, ω represents the angular frequency, t is the time interval, $\boldsymbol{x}$ is the unit vector at x axis. An approximate dipole is formed since electron clouds are displaced driven by the external electric field.[46] Dipole moment $\boldsymbol{p}$ is linearly proportional to $\boldsymbol{E}$, as defined by

$$\boldsymbol{p} = \varepsilon_m \alpha \boldsymbol{E} \quad (2)$$

where α is dipolar polarizability, ε_m is the medium dielectric constant. The polarizability is related to other parameters by

$$\alpha = (1+\kappa)\varepsilon_0 V \frac{(\varepsilon-\varepsilon_m)}{(\varepsilon+\kappa\varepsilon_m)} \quad (3)$$

where ε_0 is the permittivity of vacuum, V is the nanoparticle's volume, ε is the dielectric function, κ is a shape-dependent variable embodies surface geometric polarizability.[50] The value of κ equals to 2 for a nanosphere, and it is larger for other shapes with higher surface curvature. Dielectric function $\varepsilon(\omega)$ is definded by its interband transitions ε_{ib}, electron collision frequency γ, bulk plasma frequency ω_p, effective mass m_e and density of free electrons n_e.[32] These

equations point out that the polarizability of dipoles is determined by the nanoparticle's shape, size, electrons distribution and the surrounding dielectric environment.[32]

The optical behaviors of metal nanostructures can be expressed by solving free electron response. In Equation 3, when $|\varepsilon + \kappa\varepsilon_m|$ is minimum, the polarizability becomes maximum as resonant enhancement at

$$\mathrm{Re}[\varepsilon(\omega)] = -\kappa\varepsilon_m \quad (4)$$

where Re represents the real part.[50] This frequency ω_{LSPR} corresponds to the LSPR frequency of the nanoparticle, and the solution of ω_{LSPR} is as given by

$$\omega_{\mathrm{LSPR}} = \sqrt{\frac{n_e e^2}{m_e \varepsilon_0 (\varepsilon_{ib} + \kappa\varepsilon_m)}} \quad (5)$$

As a result, the LSPR frequency highly depends on the bulk plasma frequency ω_p, morphology of nanoparticle κ, and the surrounding medium ε_m.[16]

The resonant enhancement of optical response appears as enhanced light absorption and scattering. As calculated by Poynting vector, the corresponding cross sections for absorption and scattering in a nanosphere are expressed as

$$C_{\mathrm{abs}} = k\mathrm{Im}[\alpha] = 4\pi k a^3 \mathrm{Im}\left[\frac{\varepsilon - \varepsilon_m}{\varepsilon + 2\varepsilon_m}\right] \quad (6)$$

$$C_{\mathrm{sca}} = \frac{k^4}{6\pi}|\alpha|^2 = \frac{8\pi}{3} k^4 a^6 \left|\frac{\varepsilon - \varepsilon_m}{\varepsilon + 2\varepsilon_m}\right|^2 \quad (7)$$

where $k = 2\pi/\lambda$ as the wavenumber, a is the radius of nanosphere, and Im represents the imaginary part.[5,46] Extinction cross-section of the nanoparticle C_{ext} equals to the sum of cross-sections of absorption and scattering. Approximatively, at the resonant frequency, C_{ext} is maximized for efficient harnessing of external light with wavelength at the plasmonic band. Light absorption and scattering ability will be changed according to the polarizability of dipoles as well as the morphology factor and dielectric function of the nanoparticle. For a nanoparticle with very small a, the efficiency of absorption dominates over scattering due to a smaller exponent of a in absorption cross-section.[18] As an example, Figure 2c shows the simulated

extinction spectra of Au nanospheres with radius of 20 nm and 50 nm through discrete dipole approximation (DDA) method.

EM field distribution is another key factor for plasmonic applications. Under quasistatic limit, the solution of Laplace equation can be used to describe the distribution of the electric field.[16] The internal field is solved to be homogeneous over the whole volume of the nanosphere as

$$\boldsymbol{E}_{\text{in}} = \frac{3\varepsilon_m}{(\varepsilon+2\varepsilon_m)}\boldsymbol{E}_0 \qquad (8)$$

The electric field outside the sphere at $\boldsymbol{r} = r\cdot\boldsymbol{n}$ is expressed by

$$\boldsymbol{E}_{\text{out}} = \boldsymbol{E}_0 + \frac{3\boldsymbol{n}(\boldsymbol{n}\cdot\boldsymbol{p})-\boldsymbol{p}}{4\pi\varepsilon_0\varepsilon_m}\cdot\frac{1}{r^3} \qquad (9)$$

where r is the distance to the center of sphere, and $\boldsymbol{n}$ represents the unit direction vector.[16] Equation 9 involves external EM field $\boldsymbol{E}_0$ and the EM field aroused by dipole polarization. The term $1/r^3$ shows that the dipole field decay rapidly when moving away, and the enhancement of electric filed is localized at the vicinity of the surface. The condition for resonance in dipolar polarizability α to meet Equation 4 also leads to concomitant resonant enhancement of both the internal and dipolar electric fields. Therefore, in the resonance condition $\text{Re}[\varepsilon(\omega)] = -\kappa\varepsilon_m$, the ratio of $(|\boldsymbol{E}|/|\boldsymbol{E}_0|)^2$ is maximum.

2.2 Plasmonic Coupling between Metal Nanostructures

For a nanoparticle in an external electric field $\boldsymbol{E}_0$, the near-field enhancement by dipole field is decayed along with farther distance away from the nanoparticle surface by $1/r^3$. A multipole expansion of possible modes can be used to describe the near-surface electric field as

$$\boldsymbol{E}_{\text{nf}} = \frac{2\alpha\boldsymbol{E}_0}{4\pi\varepsilon_0 r^3} + \frac{3\beta\dot{\boldsymbol{E}}_0}{4\pi\varepsilon_0 r^4} + \frac{4\gamma\ddot{\boldsymbol{E}}_0}{4\pi\varepsilon_0 r^5} + \cdots \qquad (10)$$

where α, β, γ, … are the multipole polarizability tensors of the nanoparticle represent dipole, quadrupole, octupole, …, respectively.[32] When two nanoparticles get close to each other with

a narrow gap, plasmonic coupling is established through strong interaction between individual plasmonics. Each nanoparticle is affected by the near-field radiation of another neighbouring nanoparticle along with external electric field $\boldsymbol{E}_0$, as

$$\boldsymbol{E} = \boldsymbol{E}_{\mathrm{nf}} + \boldsymbol{E}_0 \qquad (11)$$

Figure 3a and b illustrate the near-field interaction between the nanoparticles.[51] In this coupled system, the net electric field experienced by each nanoparticle combines the external radiation and the dipole fields of other nanoparticles, which is distance-dependent as Equation 10, polarization and orientation-dependent as Equation 9. The collective plasmonic resonances are impacted due to redistribution of the electric field, and meanwhile, the resonant frequency shifts. As such, the plasmonic coupling is determined by the distance between each nanoparticle, polarization and orientation of each dipole (to be discussed in the next section).[43] In addition, for nanoarrays with interparticle distance on the order of incident light wavelength, far-field plasmonic coupling dominates in the coupled nanostructures with r^{-1} dependence, but can be hardly used in solar-driven reactions.[52]

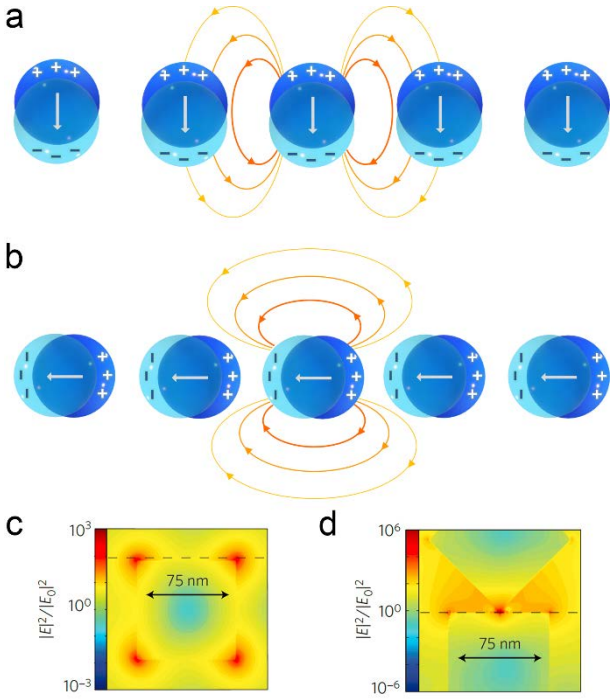

Figure 3. a,b) Schematic illustration of near-field coupling between metal nanoparticles with two different polarization directions. c,d) Simulated spatial distribution of EM field enhancement of a 75 nm Ag NC and two 75

nm Ag NCs separated with 1-nm distance, respectively. c,d) Reproduced with permission.[9] Copyright 2011, Springer Nature.

The exciton-coupling model for dimerized organic chromophores may be applied to explain the plasmonic coupling between two metal nanoparticles.[32,44] The net electric field of each dipole can be described by the incident field and the other dipole field:

$$\boldsymbol{E} = \boldsymbol{E}_0 + \frac{\xi \boldsymbol{p}}{4\pi\varepsilon_0 r^3} \quad (12)$$

where $\boldsymbol{p}$ is each dipole. And ξ is the orientation parameter of axis and direction of dipole as expressed by

$$\xi = 3\cos\theta_1 \cos\theta_2 - \cos\theta_{12} \quad (13)$$

where θ_1 and θ_2 are the angles between the inter-dipole axis and the direction of each dipole, θ_{12} is the angle between these two dipoles' directions. The energy splitting $2U$ can be calculated to describe the interaction energy between the two organic molecules, analogous to the Coulombic interaction between the dipole moments.[43] From Equation 12, the interaction energy U is calculated as

$$U = -\frac{\xi|\boldsymbol{p}|^2}{4\pi\varepsilon_0\varepsilon_m r^3} \quad (14)$$

Equation 12 and 14 are applicable for the aggregation of molecules, and the size of molecule is small compared to the distance of the dimer. These equations could be used to express the impact of orientation and polarization on plasmonic coupling. For incident light polarization along the inter-dipole axis, ξ equals to 2, which implies a negative value of U and an attraction force between the dimer, leading to a red-shift of the resonant frequency in the dimer. If the polarization is orthogonal to the axis, ξ equals to -1, which results in repulsive interaction energy and a blue-shift of the resonant frequency.[31] We discuss the above near-field plasmonic coupling based on the simplest mode, nanosphere dimer. For the nanostructures of different configurations, the electric field distribution of each component varies according to

alteration of related factors, such as components, shape factor κ, dipolar polarizability α, direction $\boldsymbol{n}$, and orientation parameter ξ. As shown in Figure 3c and d, plasmonic coupling induced EM field enhancement increases by 10^3-fold in the Ag NCs dimer as compared with an isolated Ag NC due to the strong plasmonic coupling effect.[9] Based on relevant equations, the collective plasmonic coupling resonances, the interaction between each component, the corresponding resonant frequency and optical performance are dominated by the configuration of coupled metal nanostructures.[52,53]

To investigate the optical performance and EM field distribution of coupled metal nanostructures, related modeling solutions of coupled nanostructures could be built on the basis of the dipole−dipole coupling models.[54] Many simulation methods have been developed to study the plasmonic coupling effect, including DDA,[55] generalized multiparticle Mie theory (GMM),[51] boundary element method (BEM),[33] finite element method (FEM),[56] finite-difference time-domain method (FDTD) and surface integral equation method (SIE).[57,58] These methods can simulate the light extinction spectra of the coupled nanostructures and the EM field distribution in the vicinity of the coupled nanostructures by applying different conditions. Experimentally, we can use UV-vis extinction spectroscopy, reflectance spectroscopy, absorption spectroscopy, and dark-field scattering spectroscopy to analyze the light extinction of the coupled nanostructures.[59-61] Besides, the scanning transmission electron microscopy (STEM)–electron energy loss spectroscopy (EELS) mapping technique and photoemission electron microscopy can also be used to visualize the spatial distribution of near-field plasmonic coupling.[58,62,63]

2.3 Regulation of Plasmonic Coupling

Based on the above discussion, the polarization of incident light, the orientation of dipoles, and spacing between the coupled nanostructures will all affect the plasmonic coupling

resonances and related performance.[43] As such, this section will discuss the effect of different parameters on the regulation of plasmonic coupling.

2.3.1 Distance

Distance between the coupled metal nanostructures is the key factor for plasmonic coupling. As explained in section 2.1 and 2.2, both the near-field of isolated nanoparticle and the interaction between coupled nanoparticles decrease with the enlarged distance.[31,32] As a result, the resonant optical performance and hybridized electric field are distance-dependent in the plasmonic coupling system.[64-66] **Figure 4**b and c show the experimental micro-absorption spectra and calculated extinction spectra of Au nanodisc dimers prepared by electron beam lithography (EBL) with a diameter of 86 nm.[39] Along with reduced interparticle distance, a strong red-shift of the extinction band was observed in the parallel polarization direction for both measured and DDA-simulated spectra. Red-shift of LSPR denotes a lower energy requirement for excitation of plasmonic coupling resonance.[32] The red-shift $\Delta\lambda$ of resonance wavelength at maximum absorption increased almost exponentially with gap reduction. Comparing with the LSPR resonance wavelength λ_0 of isolated particles, the shift fractional index $\Delta\lambda/\lambda_0$ was found exponentially correlated with the gap/diameter value (s/D) for different sizes (Figure 4d), as given by

$$\frac{\Delta\lambda}{\lambda_0} = A \cdot e^{-s/\tau D} \qquad (15)$$

where A is the pre-exponential factor, and τ is the decay constant.[39] Both A and τ depend on different conditions, such as configuration, composition and morphology of coupled nanostructures.[45] Through calculation by DDA method, A was estimated to be 0.14 ± 0.01 with $\tau = 0.23 \pm 0.03$, and the related curve in the experimental spectra was also exponentially fitted with $A = 0.10 \pm 0.01$ and $\tau = 0.18 \pm 0.02$ for 86-nm Au nanodisc dimers.[39] For tip-to-tip Au nanoprism dimers, D in Equation 15 represents the bisector size of nanoprism.[67] The

corresponding values, A = 0.13 ± 0.01, τ = 0.34 ± 0.05, were calculated based on the experimental extinction spectra.

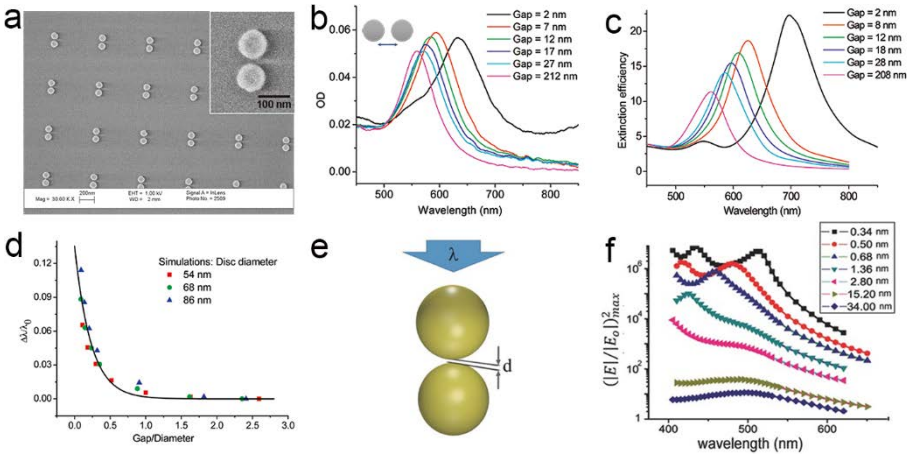

Figure 4. a) SEM image of Au nanodisc dimer arrays with diameter of 86 nm. b,c) Experimental microabsorption and calculated extinction spectra of Au nanodisc dimers with various interparticle distance under light along the interparticle axis. d) The plot of fractional LSPR red-shift $\Delta\lambda/\lambda_0$ with respect to interparticle distance (normalized by the diameter of nanodisc). e) Schematic illustration of an Ag NS dimer separated by a distance *d* under light irradiation along the interparticle axis. f) Spectral dependence of EM field enhancement $(|\boldsymbol{E}|/|\boldsymbol{E}_0|)^2_{max}$ of Ag NS dimer for different interparticle distance. a-d) Reproduced with permission.[39] Copyright 2007, ACS. e,f) Reproduced with permission.[35] Copyright 2015, Wiley-VCH.

Besides the LSPR band, distribution and enhancement of the coupled electric field are also governed by interparticle distance.[45,64,68] For two Ag NSs with a diameter of a = 70 nm separated by distance d, numerical calculations showed that the EM squared enhancement factor $(|\boldsymbol{E}|/|\boldsymbol{E}_0|)^2$ increased manifold with decreasing d under linearly polarized incident light along the interparticle axis (Figure 4f).[35] The EM field enhancement is also related to the wavelength of incident light. The coupled nanospheres with d = 0.34 nm obtained an EM enhancement factor $(|\boldsymbol{E}|/|\boldsymbol{E}_0|)^2$ of over 10^6 under monochromatic light ranging from 405 to 530 nm. These results demonstrate that the coupled nanoparticles with very small distance could establish extremely strong plasmonic coupling and remarkable EM field enhancement.[68]

2.3.2 Polarization

The polarization of external electric field will influence the plasmonic coupling as described by Equation 11.[31] For the simple Au nanodisc pair, Figure 4b shows the absorption spectra under external light parallel polarized along with the interparticle axis.[39] The interaction is attractive in this situation with a negative *U*, leading to lower plasmonic frequency. In contrast, when the polarization direction of external EM field is perpendicular to the interparticle axis, a slight blue-shift appears along with reduced distance as shown in the micro-absorption spectra (**Figure 5**a), which results from the repulsive interaction between the dipoles as explained in section 2.2.

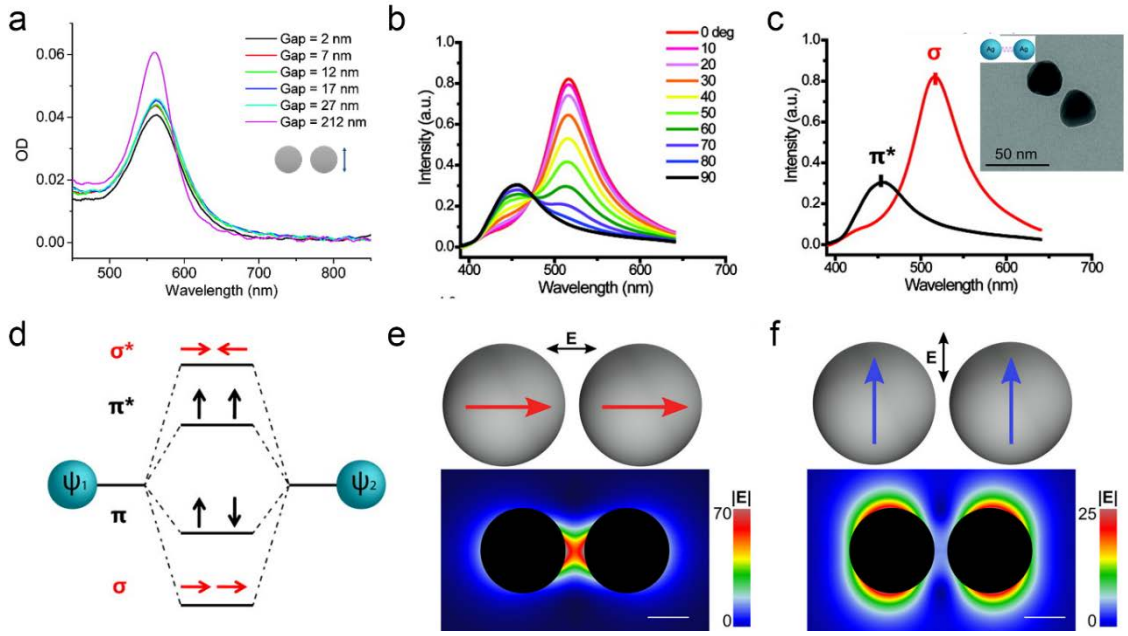

Figure 5. a) Experimental microabsorption spectra of Au nanodisc dimers with various interparticle distance under polarized light perpendicular to the interparticle axis. b) Simulated scattering spectra of Ag NP dimers with different polarizer angles. c) Hybridization model of σ-like and π*-like plasmonic coupling in accord with polarizer angles at 0° and 90°. Insert is the TEM image of an Ag NP dimer. d) A coupled dipole-dipole model of symmetric dimer in the quasistatic approximation. e,f) Plasmon coupling schematic and simulated EM field distribution in spherical dimers with small gaps with light polarized along (e) and across (f) the dimer axis, respectively. a) Reproduced with permission.[39] Copyright 2007, ACS. b-d) Reproduced with permission.[69] Copyright 2010, ACS. e,f) Reproduced with permission.[70] Copyright 2016, ACS.

LSPR scattering spectra of symmetric 40 nm Ag NP dimers are shown in Figure 5b.[69] With the increase of polarization angle from 0° to 90°, the scattering peaks of symmetric Ag dimer shift distinctly from 517 nm to 456 nm, indicating that the longitudinal coupling of LSPR owns lower energy and transverse coupling is endowed with higher energy. This LSPR coupling is similar to the formation of bonding and anti-bonding modes as described in section 2.2.[53] Figure 5d displays the hybridization model of a coupled dipole−dipole model, which approximatively matches with experimental results at the polarization angle of 0° and 90°.[69] For σ*-like and π-like plasmonic coupling in symmetric dimers, the net dipole moment equals to 0, so these two modes are optically dark.

Consistent with the resonant optical performance, the coupled EM field distribution is impacted by the polarization of external light. When the polarization direction of external EM field is along the interparticle axis, a strongly confined and intense EM field arises in the gap due to the constructive interference between the dipoles (Figure 5e), along with a red-shift of LSPR band.[70] For the transverse coupling, the dipoles interfere destructively, leading to a less intense EM filed in the gap (Figure 5f) and a blue-shift of plasmonic band. The findings point out that polarization-dependent resonance frequency and EM field could be manipulated by modulating the incident light.[71,72]

2.3.3 Orientation and Configuration

For anisotropic nanostructures, orientation or configuration of the coupled nanostructures determines the approximate dipole moment ***p*** and the interaction between nanostructures, and thus will impact the plasmonic coupling resonances.[40,43] When one Au nanorod rotates in a nanorod dimer, the plasmonic band is blue-shifted with the increase of rotation angle due to the damped coupling interaction between the dipoles, accompanied by a decrease of extinction intensity.[44] Similarly, different configurations of Au nanorod dimers also exhibited changeable

extinction spectra and surface charge density.[73] According to DDA calculation, the plasmonic coupling of Au nanorod dimers is both distance-dependent and orientation-dependent. Both red-shift and blue-shift were found in plasmonic coupling resonant frequency, consistent with the hybridization model of different configurations in DDA simulations.[73]

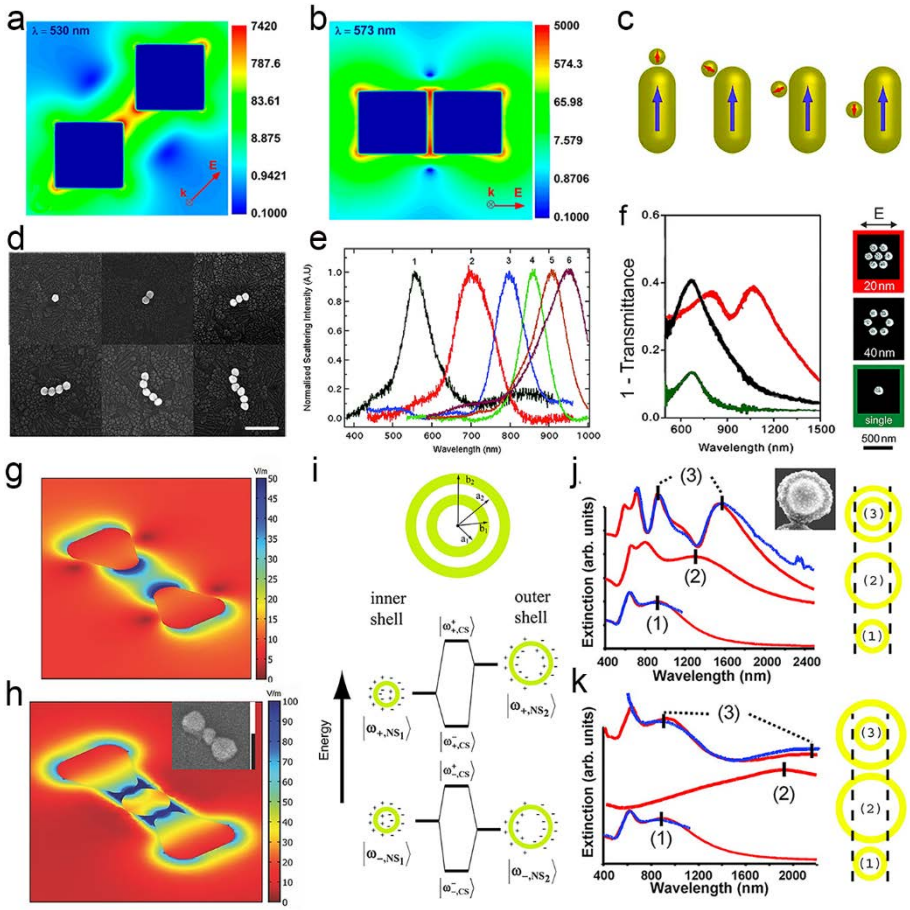

Figure 6. a,b) Calculated EM field distributions of Ag NC dimers (a) edge-to-edge and (b) face-to-face configuration under polarized light along the interparticle axis. The distances are 11 nm and 2 nm, respectively. c) Schematic of Au nanorod-nanosphere heterodimers and corresponding dipoles. d,e) SEM images and normalized experimental scattering spectra of Au NS chain with different numbers of NS. Scale bar = 250 nm. f) Experimental extinction spectra and corresponding SEM images of Au oligomers. g,h) Simulated EM field distribution in bowtie-like nanostructures before and after binding with a nanosphere. Insert is the SEM image of nanobowtie. Scale bar = 100 nm. i) Diagrams of the dual shell nanostructures and the energy level diagram describing the interaction between the inner- and outer-nanoshell plasmonic resonances. j,k) Experimental (blue) and theoretical (red) extinction spectra for concentric nanoshells (3) compared to the inner (1) and outer (2) nanoshell plasmon resonance in different-strength coupling regimes. a,b) Reproduced with permission.[45] Copyright 2016, ACS. c)

Reproduced with permission.[74] Copyright 2012, ACS. d,e) Reproduced with permission.[33] Copyright 2011, ACS. f) Reproduced with permission.[40] Copyright 2010, ACS. g,h) Reproduced with permission.[71] Copyright 2014, Wiley-VCH. i-k) Reproduced with permission.[75] Copyright 2003, American Association for the Advancement of Science.

Orientation and configuration of coupled metal nanostructures could also affect the coupled EM field distribution. Calculated EM field distributions of Ag nanocube dimers with face-to-face or edge-to-edge configuration are shown in **Figure 6**a and b.[45] The edge-to-edge dimers with a distance of 11 nm exhibit a two-fold stronger EM field intensity in the interparticle gap than that of face-to-face dimers with a smaller distance. Distance-dependent extinction spectra indicated the exponential relations of fractional LSPR red-shift index $\Delta\lambda/\lambda_0$ and dimer distance were diverse for these two configurations. Compared to edge-to-edge dimers, the large surface area of face-to-face dimers dilutes the confinement of dipole oscillation near the gap.[76] When the coupled nanostructures are not symmetric, configurations could regulate the plasmonic coupling accordingly.[59] Analogous dipole−dipole coupling varied with different configurations of Au nanorod–nanosphere heterodimers as indicated by experimental and calculated scattering spectra.[74] FDTD simulation of dipole−dipole model indicated that the dipole of nanosphere would rotate around the nanorod dipole to attain satisfactory attraction in these heterodimers (Figure 6c).

Introduction of new components in coupled nanostructures will adjust the correlated plasmonic coupling effect.[56] As shown in experimental scattering spectra (Figure 6d and e), the plasmonic band of Au NS chain shifts from 560 to 950 nm as the number of nanospheres increases from 1 to 6, which indicates lower energy of plasmonic coupling resonance.[33] In different ways of organization, the Au monomer, hexamer and heptamer exhibit different extinction spectra, as shown in Figure 6f.[40] The LSPR resonance of central nanoparticle hybridizes with the coupled resonance of the surrounding hexamer, leading to the

transformation of corresponding extinction spectra and EM filed distribution. When placing a nanosphere in the gap between a triangular-prism dimer, a bowtie-like coupled nanostructure is formed, accompanying with over 28 times enhancement of localized EM field (Figure 6g and h).[71] As such, we believe that the configuration control could be used to generate plasmonic hot spots with strong EM field and satisfactory resonance frequency for sensors and photocatalysis.

Another typical coupled configuration is core–shell nanostructure. The coupling strength is controlled by the thickness and spacing of the shell layers.[75] For example, the plasmonic band of silica–Au core–shell nanostructure red-shifts with increased thickness of the Au shell. The calculated shift fractional index $\Delta\lambda/\lambda_0$ of this core–shell nanostructure is also exponentially fitted with the shell thickness/core radius.[77] Experimental and theoretical extinction spectra of concentric silica–Au multi core–shell nanostructures exhibit strong plasmonic coupling with hybridization and splitting. The plasmonic coupling in these multi core–shell nanostructures was analogous to the hybridization of bonding and anti-bonding mode (Figure 6i).[75] As the thickness of dielectric spacing layer between Au dual shells increases, the plasmonic coupling gets damped towards disappearance (Figure 6j and k). In addition, multi-interfacial plasmonic coupling could be shaped in Au/AgAu hybrid nanostructures.[78] The LSPR extinction peak red-shifts from 524 to 576 nm with enhanced intensity as the number of layers increases. These multigap structures provide abundant adjustable parameters for interfacial plasmonic coupling, which could induce efficient photon absorption and EM field enhancement for enhanced photocatalysis.

2.3.4 Composition and Medium

Equation 2 and 3 manifest that the dielectric function of metal nanostructure $\varepsilon(\omega)$ and medium dielectric constant ε_m determine the dipole moment $\boldsymbol{p}$ and correlated LSPR features.

As such, both the composition of coupled nanostructures and the surrounding medium are critical for plasmonic coupling resonance.[64,79] As an example of composition effect, comparing with the symmetric 40 nm Ag NP dimer in section 2.3.2, the asymmetric dimer of an Ag NP and an Au NP present two scattering peaks at about 450 nm and 570 nm, resulting from the emerging σ*-like and π-like bonding in the asymmetric coupled dipole−dipole model.[69] Plasmonic coupling in this asymmetric dimer leads to red-shifts of LSPR resonances to lower energies. For self-assembled Au superlattices of different morphology and sizes, distance-dependent experimental extinction spectra show diverse shifts and extinction splittings due to strong plasmonic coupling.[80] Many other transition metals, like Pt, Pd, Cr and Ni, could also be activated for plasmonic coupling according to experimental and calculation results, enriching the opportunities of composition regulation of coupled nanostructures.[81]

Polymers, DNA, graphene, Al_2O_3, SiO_2 and MoS_2 can all be used as dielectric spacing layers to separate the coupled nanostructures.[35,37,65,82] Owing to the different dielectric constant, these spacing layers can significantly influence the plasmonic coupling effect. For example, poly(3-hexylthiophene) as a resonant absorptive layer is beneficial to the coupling between Au NPs and Au film, while the non-resonant poly(9,9-dioctylfuorene) layer does not show influence on this coupling.[83] Plasmonic coupling frequencies of core–shell nanostructures are determined by the dielectric spacer layer and the plasmonic resonances of the individual components.[75] The experimental and simulation studies have proved that the red-shift magnitude of the LSPR band in core–shell nanostructures increases linearly with the increase of ε_m.[50] From the perspective of practical applications, the composition of coupled nanostructures and surrounding medium could serve as additional regulatory factors for controlling plasmonic coupling besides distance, polarization, orientation and configuration.

3. Design and Manipulation of Structures for Plasmonic Coupling

According to section 2.3, through regulation of spacing, orientation, configuration, composition and surrounding medium of coupled nanostructures, we can tune the plasmonic coupling effect and correlated optical performance and EM field distribution.[53,84] Many experimental and theoretical studies have revealed the relations between these factors and the coupling LSPR behaviors.[34] Therefore, in order to achieve desirable plasmonic coupling effect, we could rationally design and manipulate the coupled nanostructures, which will be discussed in this section by presenting relevant "top-down" fabrication and "bottom-up" synthetic strategies.

3.1 Nanofabrication

Nanofabrication is a popular approach to create coupled nanostructures with controllable morphology, configuration and spacing, which is ideal for tuning plasmonic coupling effect.[85,86] From the perspective of application for solar-driven reactions, nanofabrication may be suitable for preparing metal nanoarrays on a conductive substrate, which is favorable for photocatalysis and photoelectrocatalysis. In this section, we would like to introduce some representative nanofabrication methods of coupled metal nanostructures.

3.1.1 Electron Beam Lithography (EBL)

EBL technology has become one advanced method to fabricate coupled metal nanostructures after development for decades.[31] EBL applies focused electron beam (e-beam) writing on e-beam sensitive resists to realize patterning. Subsequently, the exposed or non-exposed region of these sensitive resists can be selectively removed. Polymethyl methacrylate (PMMA) is a commonly used positive resist, and hydrogen silsesquioxane (HSQ) is a typical negative resist.[44,87] Through evaporation or sputtering deposition of metal on the patterned resists, metal nanostructures are created on the substrate. The followed lift-off procedure and

etching process will enable pattern transfer to different surfaces. The general nanofabrication procedures for coupled metal nanostructures are shown in **Figure 7**a, including i) spin-coating of resist onto a substrate (e.g. glass, silicon, Si_3N_4, etc.), ii) EBL exposure and development, iii) metal deposition, iv) pattern transfer and post-treatment.[85]

As described in section 2, the principles of plasmonic coupling effect have been experimentally demonstrated by the representative coupled nanostructures, such as Au nanodisc dimer and nanorod dimer, fabricated by EBL.[31,39] The resists can be patterned diversely by using a pattern generator in EBL. Then after lift-off and etching processes, various patterns of coupled metal nanostructures can be fabricated with different shapes, sizes, spacing and orientation, including Au oligomer nanoarrays, Au nanochains, Au V-shaped nanoantennas, and Pt, Pd, Cr, Ni nanorod dimers.[40,63,81,87] The sequences of pattern transfer process in the lift-off procedure and the etching process may be different. For etching transfer, the metal film is deposited on the substrate prior to spin-coating of resist, followed by e-beam exposure and etching process.[64] The spatial resolution of EBL is ~10 nm limited by the e-beam size, electron scattering and the metal grain size.[64] In addition, the thickness of the patterned metal nanostructures will also influence the plasmonic coupling effect. In short, the EBL technology provides a delicate platform for design and fabrication of planar patterns of coupled metal nanostructures with precise control over the feature size, morphology and spacing.[85]

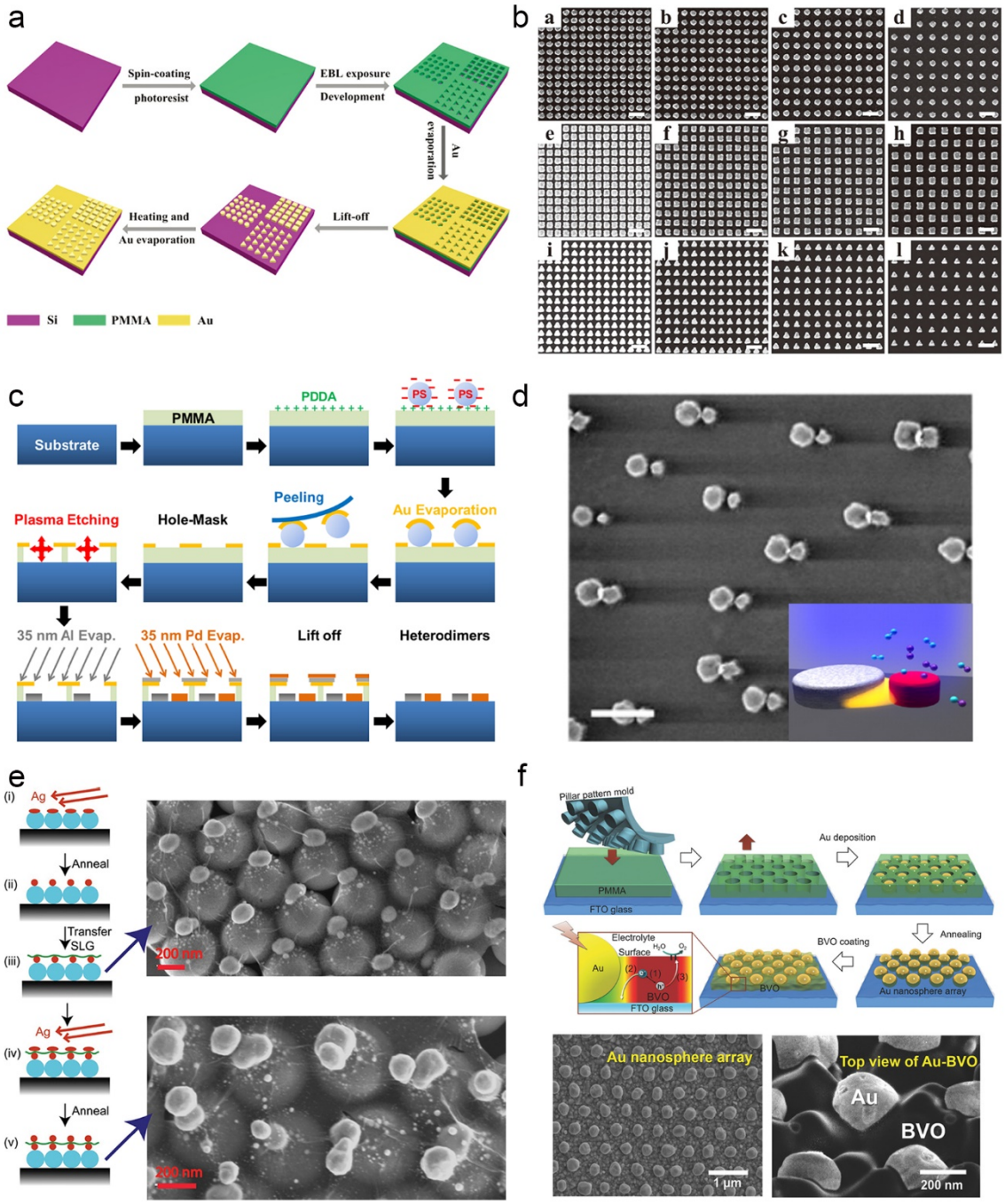

Figure 7. Schematic diagrams of different fabrication processes and corresponding SEM images of plasmonic nanoarrays: a,b) EBL process and SEM images of Au nanoarrays. Scale bar = 300 nm. c,d) Hole-mask lithography process and SEM image of Al-Pd nanodisc arrays. Scale bar = 200 nm. e) Oblique angle deposition process and SEM images of Ag-graphene-Ag nanoarrays. f) patterned template deposition process and SEM images of Au-$BiVO_4$ nanoarrays. a,b) Reproduced with permission.[85] Copyright 2015, The Royal Society of Chemistry (RSC). c,d) Reproduced with permission.[88] Copyright 2016, ACS. e) Reproduced with permission.[35] Copyright 2015, Wiley-VCH. f) Reproduced with permission.[89] Copyright 2018, Wiley-VCH.

3.1.2 Nanosphere Lithography

Nanosphere lithography (NSL) is a technology combining self-assembly of nanospheres and pattern transfer to produce metal nanoarrays of periodic two-dimensional (2D) patterns.[90,91] The self-assembled monolayer of polystyrene (PS) or silica nanospheres on a substrate acts as the lithography mask, and can be formed through different methods such as Langmuir–Blodgett, dip coating, solvent evaporation, and air/liquid interface assembly.[53,60] After metal deposition and lift-off procedure, different patterns can be generated on the substrate, such as Au nanohole array, Au@TiO_2 nanobowl array, hexagonal Ag NPs@Au nanobowl array, and Ag triangular nanoarrays.[57,91-93] The feature size and spacing can be controlled via adjusting the size and distribution of the template nanospheres. Further, the created metal nanohole array could also be used as a mask for fabrication of other nanostructures. Figure 7c shows the fabrication process of Al−Pd nanodisc heterodimer arrays through a hole-mask lithography method.[88] The Au nanohole array was used as the mask, then Al−Pd heterodimers were fabricated through etching, oblique evaporation of Al and Pd, and lift-off processes. Although the spatial resolution of NSL technology is usually above 100 nm, which is limited by the size and distribution of nanospheres, it provides an economic way to prepare large-scale coupled metal nanostructures.

3.1.3 Other Nanofabrication Methods

Based on the patterning-based lithographic technology, other nanofabrication methods have been developed to produce coupled metal nanostructures. For instance, programmable DNA self-assembly was employed as the mask for patterning of coupled plasmonic nanostructures.[94] In this method, DNA origami silhouettes were drop-casted on the substrate, followed by deposition and etching of SiO_2 and metal film, to generate DNA shaped metal

nanostructures. Another example is oblique angle deposition combining graphene transfer for fabricating coupled metal nanoparticle arrays.[35,95] As illustrated in Figure 7e, monolayer graphene as the spacing layer of coupled Ag NPs established extremely large and localized EM field and 100-fold enhancement of photoresponses.[35] This method can be employed on other 2D materials as thin spacers between coupled metal nanostructures. In addition, the patterned nanostructures can also be used as templates to prepare nanoarrays for plasmonic coupling (Figure 7f).[89] These methods enable the diversity and adjustability of coupled nanostructures.

3.2 Controllable Colloidal Synthesis

Controllable colloidal synthesis is a type of bottom-up method for preparing coupled metal nanostructures of different morphology, size and composition.[96] Monocomponent metal nanostructures with tunable plasmonic coupling effect, such as Au nanoframes, Au nanocages and Au NP clusters, can be prepared via different colloidal synthesis methods.[97-100] External and internal plasmonic resonances will hybridize to establish strong plasmonic coupling in these nanostructures.[99] For example, Han et al. synthesized Au particle-in-a-frame nanostructures with sub-2 nm nanogaps using the galvanic replacement method, which could generate 57.5 times enhanced EM field due to the plasmonic coupling effect.[97]

Controllable colloidal synthesis is particularly suitable for the fabrication of core–shell nanostructures. As described in section 2.3, core–shell metal nanostructures could be applied for attaining plasmonic coupling effect. Comparing with metal nanoarray or oligomers, core–shell nanostructures hold unique intrinsic structural features,[75] which allow us to control the composition and thickness of both core and shell materials to achieve optimal plasmonic coupling effect for efficient light harvesting and strong EM field enhancement.[77] For example, Au multimer@MoS_2 core–shell nanostructures were prepared via a hydrothermal approach by using surface-functionalized Au multimers (**Figure 8**a).[101] Broadened plasmonic absorption

and stronger near-field enhancement were observed for the Au multimer@MoS_2 core–shell nanostructures as compared with Au monomer@MoS_2 core–shell nanostructures.

Seed-mediated growth and galvanic replacement are appropriate methods for the synthesis of multicomponent core–shell and some other coupled nanostructures,[79] such as Au@Ag core–shell NPs,[102] Au@Ag@Au core–shell shell NPs,[103] Au@AgAu nanorattles,[38] Au@M (M = Pd or Pt) bimetallic core–shell NP assemblies,[104] Pt@Au tripod nanoframes,[105] and multi shell Au/AgAu hybrid nanostructures.[78] These coupled nanostructures possess multi-interfacial plasmonic coupling effect with abundant active sites, enhanced light trapping ability and strongly coupled near-field, which enable potential applications for solar-driven reactions.[78] Besides, polymer-assisted and template-supported synthetic methods were also employed to prepare coupled nanostructures, such as Au@SiO_2 dual shell NPs,[75] Au core–Ag satellite nanostructures,[106] Au core–satellite nanostructures,[107] Au-nanobridged NPs,[108] porous triple-shell Au nanostructures,[109] and hollow bilayer shell Au-Au/Pd/Pt nanocatalosomes (Figure 8b and c).[110] Novel plasmonic coupling properties and excellent catalytic activities were obtained by using these unique coupled nanostructures.

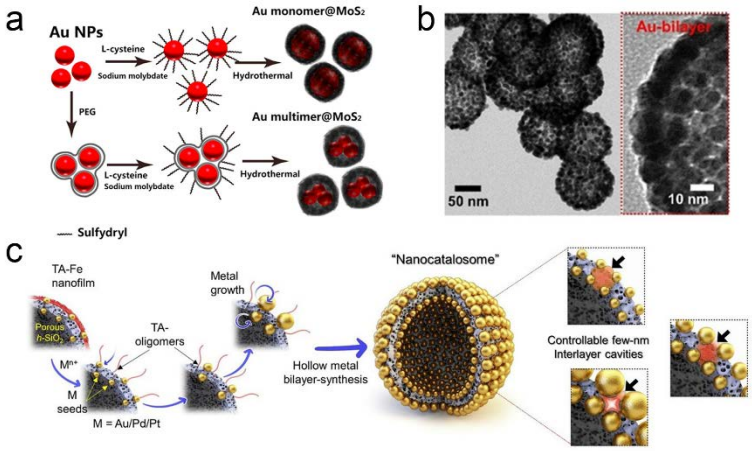

Figure 8. a) Scheme of the synthetic process of the Au multimer@MoS_2 core–shell nanostructures. b) TEM images of Au–Au nanocatalosomes. c) Scheme for the formation of hollow bilayer shell nanocatalosomes with controllable interlayer cavities. a) Reproduced with permission.[101] Copyright 2016, Elsevier. b,c) Reproduced with permission.[110] Copyright 2020, Wiley-VCH.

Through galvanic replacement, anisotropic trimetallic nanoparticles composed of Au, Ag and Cu with tunable plasmonic coupling properties could be prepared.[79] Localized intense EM field could be established at the junction area in these heterojunctions, with up to 219-fold enhancement in Cu–Au–Ag heterojunctions as compared with Au@Cu–Ag heterojunctions. This study demonstrated that the controlled colloidal method is potentially valuable for the synthesis of multicomponent nanoparticles with versatile plasmonic coupling effect. In addition, metal NPs could be decorated on the substrate surface via in-situ reduction to form coupled nanostructures, such as $Ag/ZnIn_2S_4@TiO_2/Ag$,[111] flexible substrate supported Au NPs array,[112] and Pd decorated Al nanocrystals[113]. Further development of controllable colloidal synthetic methods might provide new opportunities for exploring plasmonic coupling effect.

3.3 Self-Assembly

Self-assembly of metal nanostructures is another popular approach to organize small plasmonic nanoparticles into well-ordered combinations or superstructures,[34] and can be achieved through surface functionalization, template-assisted assembly and external field directed assembly. One can manipulate adaptable self-assemblies to control the plasmonic coupling effect of the coupled metal nanostructures by adjusting the interparticle distance, configuration, composition and formation of the assembled nanostructures.[53] Varying these parameters will change the intensity and frequency of plasmonic coupling resonance of the entire assembly structure as well as the EM field distribution, which allows us to achieve desirable optical properties and maximal EM field enhancement for practical applications in solar-driven reactions.[114]

3.3.1 Molecules Assisted Self-Assembly

During the preparation of metal NPs, capping agents, such as citrate and polyvinylpyrrolidone (PVP), are often used to passivate the surface of metal NPs.[96] Upon proper treatment, the surface of metal NPs can be further functionalized by other terminal functional groups, such as thiolated DNA and polyethylene glycol (PEG).[65,115] If any specific attractive interactions between the capping ligands of neighboring nanoparticles can be triggered in appropriate conditions (e.g. pH, solvent, temperature, etc.), spontaneous aggregation of these functionalized nanoparticles will occur to form a large assembly structure.[53] In this self-assembled structure, the distance between metal nanoparticles is determined by the length of capping ligands as the spacers.[65] As such, plasmonic coupling effect can be regulated through tailoring the surface capping ligands. For example, Yoon et al. have demonstrated the controlled self-assembly of a cetrimonium-capped Au nanocube and a 1,8-octanedithiol functionalized Au nanoparticle into a dimer.[59] The Au cube–sphere dimer exhibited much stronger plasmonic coupling effect with two-order higher near-field enhancement as compared with the Au sphere-sphere dimer. The thiolated DNA or polymer functionalized metal NPs could self-assembled into large plasmonic coupling architectures, such as Au NS chain, Au photonic crystal, Au nanovesicles and three-dimensional (3D) Ag NS clusters (**Figure 9**a), which could be used for the applications in sensors, phototherapy and photocatalysis.[13,33,72,116]

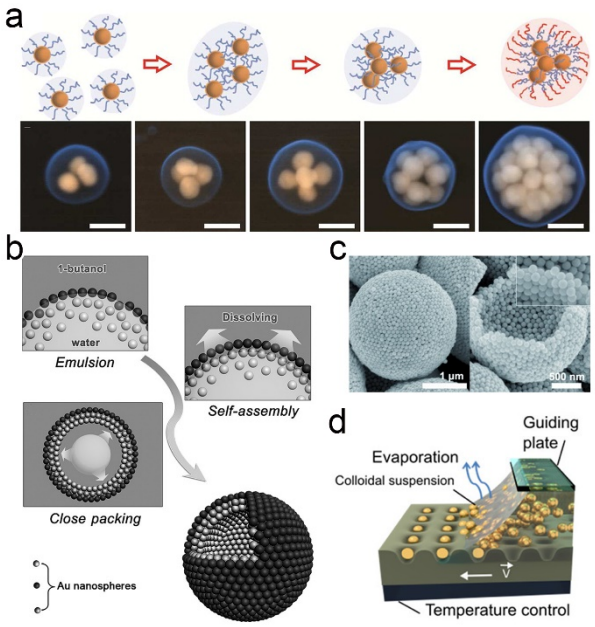

Figure 9. a) Schematic illustration of self-assembly fabrication process of 3D plasmonic nanoclusters and SEM images of clusters composed by different numbers of nanospheres. Scale bar = 100 nm. b) Interfacial self-assembly mechanism of multilayered Au colloidosomes. c) SEM images of multilayered Au colloidosomes. d) Schematic diagram of template based self-assembly. a) Reproduced with permission.[72] Copyright 2013, ACS. b,c) Reproduced with permission.[117] Copyright 2015, Wiley-VCH. d) Reproduced with permission.[118] Copyright 2019, ACS.

3.3.2 Interfacial Self-Assembly

When the surface-functionalized metal nanoparticles are located at the interface of air/liquid or two immiscible liquids, they might assemble into an ordered nanoarray through inter-particle interactions, particle-liquid interactions and interfacial tension.[60,119] The stability of interfacial self-assembly is determined by the size and wettability of the functionalized nanoparticles. The spacing and organization of nanoparticles in the assemblies can be regulated by varying surface ligands, solution pH, solvents, and other experimental conditions.[119,120] For instance, close-packed multilayer Au colloidosomes were prepared at the emulsion droplet interface of water and 1-butanol (Figure 9b and c).[117] Owing to the strong interparticle plasmonic coupling, the assembled colloidosomes exhibited an intense extinction band

spanning the entire visible light range. In another example, tunable 2D nanoarrays of Au NPs, capped with 12-mercaptododecanoic acid, could form at the planar interface of 1,2-dichloroethan and water.[121] Through controlling the withdrawn time, Ag@Au–poly-N-isopropylacrylamide NPs could assemble into 2D colloidal superstructures at the air/water interface with tunable interparticle distance and plasmonic coupling strength.[119] In addition, different-oriented 2D Ag octahedra nanoarrays can be fabricated through Langmuir–Blodgett method by controlling surface wettability of NPs at the oil/water interface.[120] In short, interfacial self-assembly of plasmonic metal nanostructures affords a convenient approach to construct plasmonic coupling nanostructures in large-scale for solar energy conversion.

3.3.3 Template Based Self-Assembly

Template based self-assembly methods combine top-down nanofabrication and bottom-up self-assembly techniques. For example, by modeling of PMMA template or polydimethylsiloxane (PDMS) soft template, metal NPs could fill the nanoholes or wrinkles of templates *via* capillary forces to form oligomers or superstructures, as shown in Figure 9d.[30,42,118] Similarly, Au oligomers could be assembled in polygonal templates of different shapes (Figure 1).[30] Besides, a flexible 2D plasmonic Au lattice was fabricated by filling Au NSs in the nanohole array of PDMS.[122] Stretch and relaxation of PDMS could shape it with uniform parallel wrinkles, then superstructures of 2D nanoarrays with continuous liner structure were formed by assembling Au NRs or Au NSs in these wrinkles.[42,123] Further, growing Au NPs on a flexible PDMS substrate could enable mechanical control of plasmonic coupling.[112,118] Overall, soft template based self-assembly of metal nanostructures might bring new opportunities to create plasmonic coupling structures in flexible devices for solar energy conversion.

4. Plasmonic Coupling in Solar-Driven Reactions

Solar-driven reaction is a sustainable strategy to convert and utilize incident photons, which can harness solar energy and store it as chemical bonds.[124] Under light illumination, semiconductor-based photocatalysts could generate electron–hole pairs as excitons in the bulk phase. Then these energetic excitons migrate to the surface and split into active electrons and holes, which initiate the redox reactions of the surface adsorbates.[9] Upon integrated with semiconductor photocatalysts, plasmonic metal nanostructures could enhance light trapping and EM field at the metal-semiconductor interface through collective oscillation of conduction electrons.[8] If coupled metal nanostructures are contacting with the semiconductor surface, as described in section 2, the light-induced plasmonic coupling could further greatly enhance the EM field at the metal-semiconductor interfaces, where the photocatalytic redox reactions would be favorably promoted. Based on this aspect, this section will focus on the roles and advantages of plasmonic coupling in solar-driven catalytic applications.

4.1 Plasmonic Photocatalysis

As mentioned above, the efficiencies of semiconductor-based photocatalysis are influenced by all of these steps including light harvesting, exciton generation, charge separation and transfer, and subsequent redox reactions.[124]. Integrating plasmonic metal nanostructures with photocatalysts can promote their light absorption, improve the charge separation and transfer, and promote their interactions with surface adsorbates.[28]

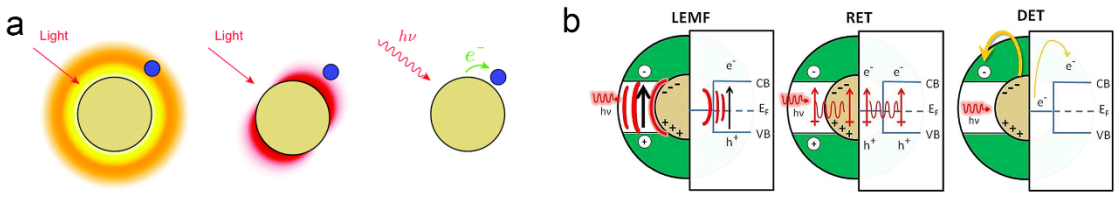

Figure 10. a) Schematic diagrams of photothermal effect, localized near-field enhancement and hot-electron excitation on a plasmonic metal nanoparticle. b) Schematic diagrams of different energy/charge transfer pathways between metal and semiconductor: local EM field enhancement (LEMF), plasmon-induced resonance energy

transfer (PIRET) and plasmon-induced hot-carrier direct electron transfer (DET). a) Reproduced with permission.[17] Copyright 2014, RSC. b) Reproduced with permission.[125] Copyright 2012, ACS.

The LSPR of metal nanostructures has two major functions, increasing light absorption at the resonant frequency and enhancing near-surface EM field.[17] In the aspect of optical performance, when the LSPR of metal nanostructures fits in the solar spectrum, it can enhance light-harvesting capability of the metal-semiconductor integrated system. The excitation of LSPR of a metal nanostructure can impact the contacted semiconductor through three typical avenues (**Figure 10**b).[4,125] One is local EM field enhancement (LEMF). The intense EM field of plasmonic metal nanostructures can significantly boost the exciton generation rate on the adjacent semiconductor surface if the plasmon resonance energy is beyond the semiconductor bandgap.[125] The second avenue is plasmon-induced resonance energy transfer (PIRET).[7] The plasmonic oscillation energy could be transferred to the semiconductor photocatalysts through the EM field or non-radiative dipole–dipole coupling, which requires spectral overlap between the metal LSPR band and the light absorption range of the semiconductor.[5] Third, upon LSPR excitation, some plasmonic hot electrons may gain sufficiently high energy that allows them to be injected into the conduction band of the adjacent semiconductor.[46,126] This process is called plasmon-induced direct electron transfer (DET), and can also initialize surface redox reactions.[28] All these processes, benefited from plasmonic metal nanostructures, can impel solar-to-chemical energy conversion through rational design.

Previous experimental and theoretical studies have demonstrated the efficacies of plasmonic metal nanostructures in various photocatalytic or photoelectrochemical (PEC) reactions including water splitting, CO_2 reduction, N_2 fixation, methane dry reforming and organic synthesis.[127-131] By combining plasmonic metal nanostructures and semiconductor photocatalysts, LSPR promoted photocatalysis can be achieved via expanding light absorption, improving charge dynamics and boosting catalytic activity.[46] Plasmonic effect can also

facilitate a variety of electrocatalytic reactions via hot electron transfer.[131] In addition, LSPR excitation may switch the product selectivity of organic reactions by enhancing adsorption of light-active molecules to alter the reaction pathway.[130]

Nevertheless, in some cases, the near-field of isolated plasmonic nanoparticles is not strong enough to dramatically promote the charge dynamics in the neighboring semiconductor photocatalysts.[101,132] One possible way to solve this issue is the manipulation of plasmonic nanostructures to establish plasmonic coupling,[52] because the coupled metal nanostructures could provide much stronger local plasmonic effect with more strengthened EM field at the metal-semiconductor interface as compared with isolated metal NPs.

4.2 Plasmonic Coupling for Photocatalysis

As described in section 2.2 and 2.3, plasmonic coupling of coupled metal nanostructures can induce significantly enhanced EM field in the spacing region,[55] and can also improve the light absorption of the integrated system according to previous experimental and theoretical studies.[70] The interparticle gapping areas of coupled nanostructures usually possess the strongest EM field due to the distance-dependent plasmonic coupling effect, and are often noted as hot spots. Multiple resonances may occur at such spatially confined hot spots, where the EM field enhancement can be orders of magnitude larger than that on the surface of isolated nanoparticles.[53] As such, these hot spots allow for higher exciton generation rates at the interface between the coupled metal nanostructures and the semiconductor photocatalysts, which are beneficial to plasmonic photocatalytic reactions.[110] In addition, a larger amount of hot electrons may exist at the hot spots, and could be injected into the molecular orbital of the adsorbed reactants to activate surface redox reactions.[62] There might be also strong interactions between the dipole moments of the adsorbed reactants and the confined EM field in the hot spots region, that can modify the chemical reaction pathways.[133]

If we separately consider the individual components in the coupled metal nanostructures, the EM field distribution and optical performance of one component will be influenced by the induced interaction of dipolar resonances with other nearby components.[134] As such, the related catalytic activity of this component could be greatly improved. These types of coupled metal nanostructures can be used for solar-driven reactions as an antenna−reactor (A−R) model. Metal nanostructures with strong LSPR activities (such as Au, Ag, Cu) behave as antennas to harvest the solar energy, while metal nanostructures with weak visible light response but excellent catalytic performance (like Pt, Pd, Ru or Rh) act as the reactors to catalyze the chemical reactions.[113] Note that spacing between the antennas and reactors is usually required to establish plasmonic coupling effect. Through plasmonic hot electrons and EM field enhancement, both optical and catalytic performance of the reactor components will be promoted.[37,113]

Table 1. Performance of plasmonic coupling for photocatalysis.

Photocatalyst	Reaction	Improved performance	EM field enhancement	Better light absorption	Enhanced charge separation	Enhanced charge transfer	Mechanism	Ref
Ag/$ZnIn_2S_4$/TiO_2	H_2 production	11-fold	4-fold	400−550 nm	√	√	PIRET	[102]
Ag/$ZnIn_2S_4$/TiO_2	CO_2 reduction	16-fold	4-fold	400−550 nm	√	√	PIRET	[102]
Au/$ZnIn_2S_4$/TiO_2	H_2 production	8-fold	1.5-fold	400−600 nm	√	√	DET	[102]
Au/$ZnIn_2S_4$/TiO_2	CO_2 reduction	12-fold	1.5-fold	400−600 nm	√	√	DET	[102]
Au@AgAu nanorattles	aniline oxidation	3.9-fold[a)]	14-fold[a)]	450−700 nm		√	DET	[38]
Au multimer@MoS_2	H_2 production	1.5-fold[a)]	√	400−600 nm	√	√		[96]
Al/Al_2O_3/Pd	HD production	~4-fold[a)]	> 10-fold[a)]	300−900 nm			A−R	[104]
Al−Pd dimers	HD production	~7-fold[a)]	√	350−700 nm		√	A−R	[88]
Au multimer/TiO_2	H_2 production	2−4-fold[a)]	28-fold[a)]	400−800 nm	√	√	DET	[122]
Au NPs/N-TiO_2 array	H_2 production	9.1-fold		350−800 nm	√	√	PIRET	[92]
Ag NPs/ZnO NRs	dye degradation	8.26-fold	8-fold	400−550 nm	√			[36]
Au@Ag/$SrTiO_3$	2-propanol oxidation	1.5-fold[a)]		400−800 nm		√		[97]

$Ag@SiO_2/Pt$	CO oxidation	1.49-fold[a)]	√	√	√	√	A−R	[37]
Au@Ag nanochains	hydrogenation	18-fold[a)]	√	600−900nm				[135]
linked Au−Au nanorod	deoxygenation	2.5-fold[a)]	√					[136]
$Au/ReS_2/Au$	H_2 production	1.5-fold[a)]	√	600−900 nm		√	A−R	[82]
$Au/MoS_2/Au$	H_2 production	2-fold[a)]	√	500−900 nm		√	A−R	[82]
$Au\text{-}TiO_2$/pNIPAM	dye degradation	~2-fold[a)]	√	√				[137]
$Pt−Au/SiO_2$	CH_4 dry reforming	1.5-fold[a)]	√	√		√	DET	[129]
$Ag/Ag_2S/BiVO_4$	organic oxidation	5-fold	√	500−800 nm	√	√		[138]
Ag/Au colloidosome	dye degradation	~1.3-fold[a)]	√	500−1000 nm		√		[139]
Au colloidosome	CO_2 reduction	1.6 μmol g^{-1}	√	500−1100 nm		√	DET	[62]
Ag nanorices/$W_{18}O_{49}$ NWs	H_2 production	6-fold	10^1−10^4-fold		√	√	DET	[140]
Au−Au nanocatalosome	alkynyl annulation	6-fold[a)]	√	√		√		[110]
Au−Pt nanocatalosome	dehydrogenation	9-fold[a)]	√	√		√		[110]
Au−Pd nanocatalosome	C-C coupling	6-fold[a)]	√	√		√		[110]
porous triple-shell Au	hydrogenation	1.5-fold[a)]	√	√		√		[109]
multigap Au/AgAu@CdS	H_2 production	47.2-fold[a)]	√	600−1100 nm		√		[78]

[a)] These represent performance comparisons with corresponding single plasmonic component.

Table 2. Performance of plasmonic coupling for photoelectrocatalysis.

Photoelectrode	Reaction	Improved performance	EM field enhancement	Better light absorption	Enhanced charge separation	Enhanced charge transfer	Mechanism	Ref
$Au\ NPs/TiO_2/Au\ NPs$	water splitting	3-fold	6-fold	450−800 nm				[141]
Fe_2O_3/Au nanoholes	water splitting	10-fold	√	450−850 nm	√	√	PIRET	[57]
Au NP/CdSe/Au film	water splitting	5-fold	> 10^4 (gap)		√	√	PIRET	[61]
$Au@SiO_2@Au\ NPs$	citrate oxidation		√		√	√	DET	[142]
Au NS array/Mo:$BiVO_4$	water splitting	2.2-fold	√	500−700 nm	√	√	PIRET	[89]
Ag NP/graphene/Cu foil	H_2O_2 generation	~1000-fold	√	400−600 nm	√	√		[143]
TiO_2/Au NPs array/TiO_2	water splitting	88-fold	√	600−1200 nm	√			[114]
Au NS array/α-Fe_2O_3	water splitting	3.3-fold	√	550−750 nm	√	√	PIRET	[144]

When integrated with semiconductor nanomaterials, coupled metal nanostructures can contribute their specialties in light trapping and charge kinetics.[111] More intensive local EM field enhancement by coupled metal nanostructures will lead to higher generation rates of

electron–hole pairs,[101] and a larger amount of energetic hot electrons that can transfer to the semiconductor.[111] Charge transfer from the coupled metal nanostructures has been directly observed by femtosecond pump-probe spectroscopy.[145]

Semiconductor nanomaterials can also act as the spacers in the coupled metal nanostructures.[82] In this situation, greatly enhanced EM field will be built at not only the metal-semiconductor interface but also throughout the entire semiconductor spacers. Consequently, the photocatalytic activities of the semiconductor spacer could be drastically enhanced.[101,132] **Table 1** and **2** present the recent examples of plasmonic coupling architectures and their effect on photocatalytic and PEC reactions, respectively. Varying configurations of coupled metal nanostructures and integrated semiconductors could lead to completely different characteristics and photocatalytic performance. Here, we will discuss different types of plasmonic coupling structures for photocatalysis.

4.2.1 Plasmonic Oligomers

Oligomer is the basic configuration of coupled metal nanostructures. As described in section 2, plasmonic coupling in the coupled nanostructures with oligomer configuration have been experimentally and theoretically studied regarding the optical performance and near field enhancement.[30,40] Au−Au nanorod dimer exhibited orientation-dependent catalytic hot-spots for deoxygenation reactions, and the one with 70° orientation angle could induce a twice enhancement factor $(|\boldsymbol{E}|/|\boldsymbol{E}_0|)^2$ in the gap region than that with 10° angle.[136] The extinction spectra of oligomers usually exhibit red-shifted and broadened LSPR band along with increased oligomer number. Meanwhile, multiple hot spots could be created in the spacing region between the individual components forming oligomers. Wei et al. demonstrated that Au multimer@MoS_2 core−shell nanostructures could show a 2.5-fold higher H_2 generation rate than Au monomer@MoS_2.[101] As shown in **Figure 11**a, the enhanced photocatalytic activity

was attributed to widened light absorption and improved charge generation and dissociation, which were induced by strong near-field coupling in the gap region between Au NPs. Similarly, Janus Au multimer−TiO_2 could present 2−4 times increase of photocatalytic H_2 evolution rate than Au monomer−TiO_2, which was ascribed to the 28-fold enhancement of local electric field, increased light absorption and more efficient generation of hot electrons (Figure 11c).[132] Indeed, plasmonic hot electrons from excited metal oligomers could trigger some chemical reactions. For example, colloidosome of 55 wt% Au loading could realize CO_2 methanation owing to hot electrons transfer from hot spots of plasmonic coupling.[62]

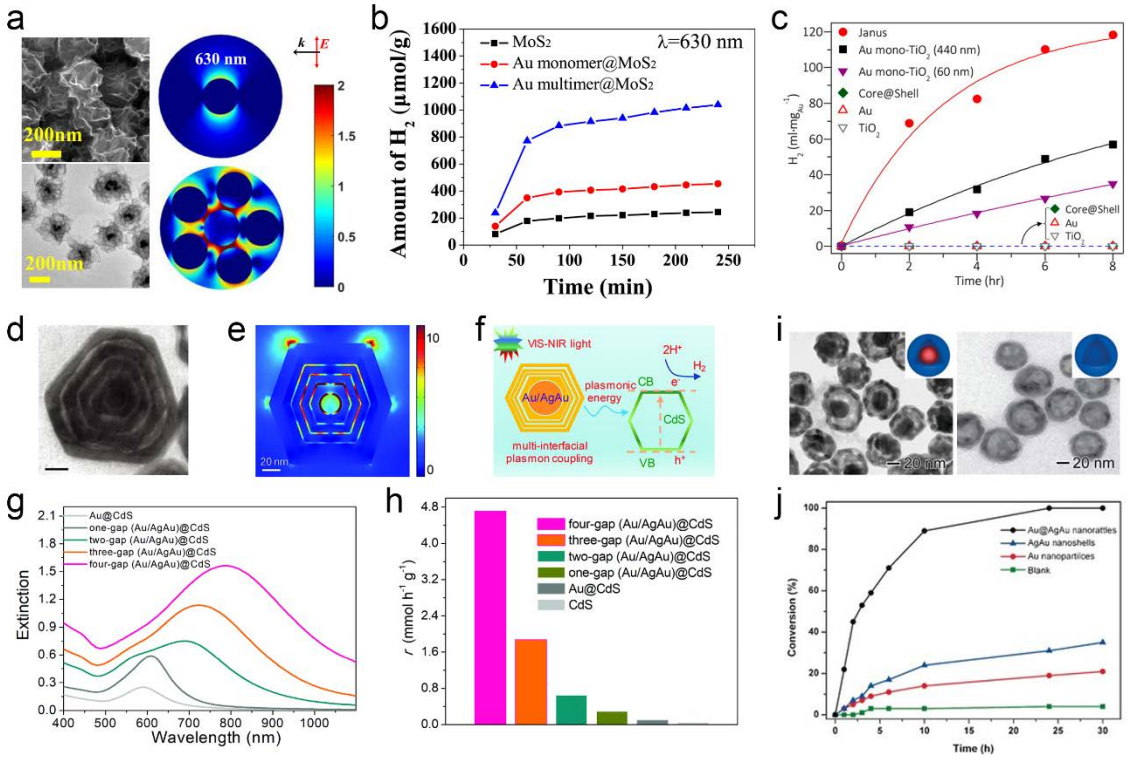

Figure 11. a) SEM and TEM images of Au multimer@MoS_2 core−shell nanostructures (left). Calculated EM field distribution of Au monomer@MoS_2 and Au multimer@MoS_2 (right). b) Time-dependent photocatalytic H_2 production profiles of MoS_2 based photocatalysts. c) H_2 evolution of Janus Au multimer−TiO_2 under visible-NIR light (λ > 420 nm) illumination. d,e) TEM image and simulated EM field distribution of four-gap Au/AgAu hybrids. Scale bar = 20 nm. f) Diagram of possible mechanism of photocatalytic H_2 production over the four-gap Au/AgAu@CdS hybrids. g,h) Extinction spectra and photocatalytic H_2 production rate of multigap CdS based photocatalysts. i) TEM images of Au@AgAu nanorattles and AgAu nanoshells. j) Conversion rate of SPR-mediated aniline oxidation by Au@AgAu nanorattles, AgAu nanoshells, and Au nanoparticles. a,b) Reproduced

with permission.[101] Copyright 2016, Elsevier. c) Reproduced with permission.[132] Copyright 2016, ACS. d-h) Reproduced with permission.[78] Copyright 2020, RSC. i,j) Reproduced with permission.[38] Copyright 2016, Wiley-VCH.

4.2.2 Core–Shell Structures

The plasmonic coupling in the core–shell nanostructures results from the hybridization of LSPR of core and shells.[75] As described in section 2.3 and 3.2, the composition, thickness and spacing will influence the plasmonic coupling effect in core–shell nanostructures and the corresponding photocatalytic activities. For example, multi-interfacial plasmonic coupling in multigap Au/AgAu@CdS is determined by the shell layer numbers.[78] The light extinction peaks of multigap Au/AgAu@CdS red-shift from 600 nm to 800 nm along with increasing shell layer numbers (Figure 11g). Photocatalytic H_2 evolution rate of four-gap Au/AgAu@CdS hybrids was 47.2 times higher than that of gapless hybrids due to the enhanced light absorption and strengthened interfacial EM field (Figure 11h). In addition, Camargo et al. studied the photocatalytic aniline oxidation over Au@AgAu nanorattles.[38] Enhanced activation of adsorbed O_2 molecules by plasmonic hot electrons and 14-fold EM field enhancement in Au@AgAu nanorattles led to 2.5-fold higher photocatalytic activity than the sum of individual AgAu nanoshell and Au core (Figure 11j).

Moreover, it is important to achieve an appropriate balance between light scattering, absorption and EM field enhancement in core–shell coupled nanostructures in order to optimize their photocatalytic performance.[37] Varying the composition of core–shell nanostructures can alter the catalytic performance for different reactions.[110] The nanocatalosome with Au−Au bilayer shells was found effective for alkynyl annulation, while Au−Pt and Au−Pd nanocatalosomes were competent for dehydrogenation and C-C coupling reactions, respectively. In these bilayer nanocatalosomes, plasmonic hot spots were formed in the narrow interparticle gaps and cavities, which could concentrate strong EM field, promote charge

generation and separation, and increase local temperature.[110] All these factors together led to the outstanding photocatalytic performance of nanocatalosomes.

4.2.3 Densely Packed NPs

When coupled metal NPs are confined in semiconductor nanostructures towards compact packing, the photocatalytic performance will be promoted. Plasmonic coupling effect of densely packed metal NPs can make up the weak absorption of certain semiconductors in the visible-NIR region.[57] For instance, after deposition of Au NPs in N-doped TiO_2 bowl nanoarrays, the photocatalytic H_2 evolution rate increased 9.1 times and 4 times under irradiation of full-spectrum light and visible light, respectively.[92] Densely packed Au NPs enabled light absorption of the integrated system above 520 nm due to the interparticle plasmonic coupling. In another example, Au NPs can self-assemble into 2D film at the air/liquid interface with a high density of sub-1 nm inter-particle gaps. When this compact Au NP-film was confined between two layers of TiO_2 films, one could achieve enhanced visible-NIR light absorption, promoted charge generation and separation, prolonged charge lifetime and 88-fold increased PEC performance (**Figure 12**a and b).[114] Further, tuning the size and distance of Au NPs could improve correlated PEC performance by strengthening plasmonic coupling effect. In the Au NS array/Mo:$BiVO_4$ photoanode, the Mo:$BiVO_4$ part located in the hot spots region between Au NSs could experience stronger light excitation through plasmon-induced resonant energy transfer (PIRET) and exhibit 2.2-fold enhancement on the photocurrent density (Figure 12c).[89]

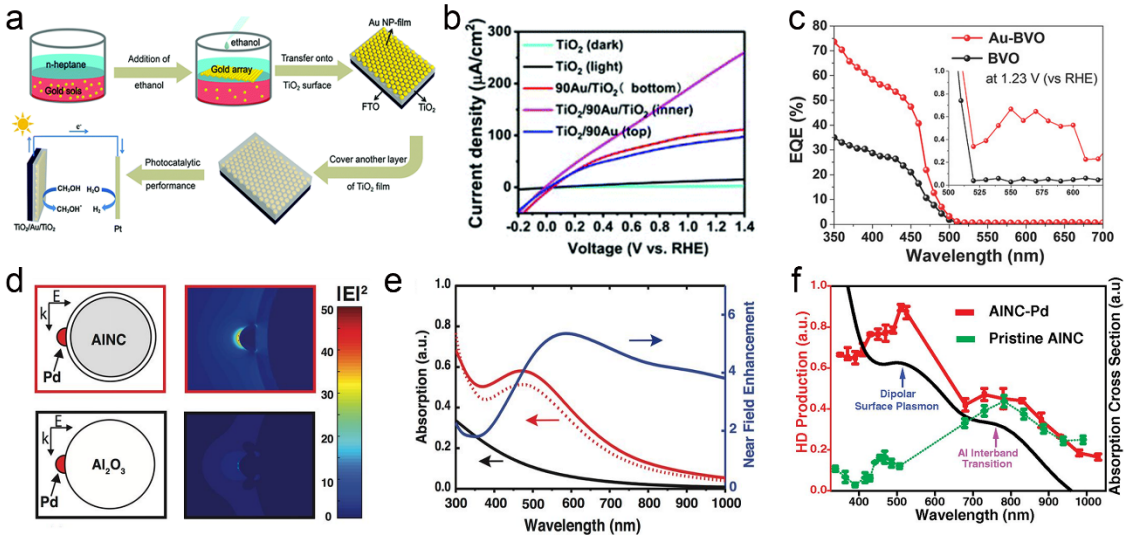

Figure 12. a) Scheme of fabrication procedures of TiO_2/Au NPs array/TiO_2 film. b) PEC performance of TiO_2 based photoelectrodes. c) External quantum efficiency spectra of Au NS array/Mo:$BiVO_4$ photoanode and Mo:$BiVO_4$ photoanode at 1.23 V vs. RHE. d) Models of Al−Al_2O_3−Pd antenna−reactor and Pd on Al_2O_3 (left) and corresponding near-field enhancement (right). e) Simulated absorption spectra of Pd on Al_2O_3 (black), Al−Al_2O_3−Pd antenna−reactor (red solid curve) and isolated absorption multiplied by field enhancement (red dashed curve). Near-field enhancement in the Al_2O_3 layer is shown in blue. f) Experimental wavelength dependence of HD production by Al−Al_2O_3−Pd antenna−reactor (red) and Pd on Al_2O_3 (green). The calculated absorption cross-section of Al−Al_2O_3−Pd antenna−reactor is shown in black. a,b) Reproduced with permission.[114] Copyright 2019, RSC. c) Reproduced with permission.[89] Copyright 2018, Wiley-VCH. d-f) Reproduced with permission.[113] Copyright 2016, The Authors, published by National Academy of Sciences.

4.2.4 Antenna−Reactor

The antenna−reactor model of plasmonic coupling provides a novel solution for solar-driven reactions. Plasmonic metal nanostructures(e.g. Au, Ag, Cu, etc.) can serve as the antennas to capture photons, and catalytic metal nanostructures (e.g. Pt, Pd, Ru, etc) can act as the reactors.[113] Through dipolar coupling interaction between the antenna and reactor, plasmonic induced hot electron transfer and EM field hot spots will promote the photocatalytic process. For example, Halas et al. reported that in a designed Al−Pd antenna−reactor system (Figure 12d), increased light absorption of Pd at 500 nm was observed due to LSPR induced

absorption enhancement.[113] The plasmonic coupling boosted the internal EM field over one order of magnitude, leading to optimized hot-carriers production and charge transfer between the Pd reactor and adsorbed reactants. Consequently, photocatalytic performance increased more than 4 times for the Pd reactor coupled with the Al antenna. Hydrogen dissociation rate was found polarization-dependent with the incident light for the oriented Al–Pd antenna−reactor pair, which is consistent with plasmonic coupling-induced absorption of Pd reactor.[88] This study demonstrated that the coupling between plasmonic metal antennas and catalytic metal reactors combined their advantages in light trapping and catalysis, and introduced coupled EM field for hot-carrier generation.[88] Similarly, decorating Pt nanoparticles onto the Ag@SiO_2 core–shell sphere surface resulted in an antenna−reactor set of Ag–Pt.[37] Upon LSPR excitation, the Ag core supply enhanced field at the Pt NP surface, which facilitated activation of adsorbed CO molecule to its promoted oxidation.

4.2.5 Semiconductor Spacers

When semiconductor materials serve as the spacers between coupled metal nanostructures, the plasmonic hot spots spatially overlap with the semiconductor spacers.[61] As discussed above, multiplied or exponential enhancement of EM field can be induced in the gap region between the coupled metal nanostructures. The strong EM field will be able to motivate energetic charge generation, separation and transfer. For example, FDTD simulations indicated that the plasmonic coupling in Ag NPs/$ZnIn_2S_4$/TiO_2 and Au NPs/$ZnIn_2S_4$/TiO_2 hybrid nanostructures lead to interfacial EM field enhancement of 4 times and 1.5 times, respectively (**Figure 13**a and b).[111] The optical response of $ZnIn_2S_4$ did not match with LSPR of Au dimer NPs, but overlapped with the LSPR of Ag dimer NPs, leading to the non-radiative PIRET induction between Ag NPs and $ZnIn_2S_4$. Indeed, both DET process by Au dimer NPs and PIRET process by Ag dimer NPs contributed to the boosted photocatalytic activities with

improved photon absorption and promoted exciton generation and separation, and prolonged charge carrier lifetime.

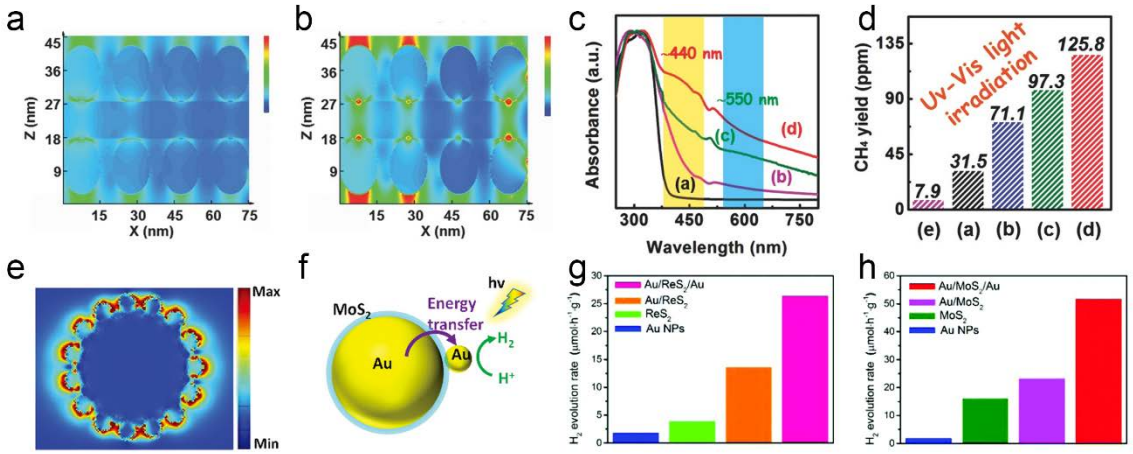

Figure 13. a,b) FDTD simulation of EM field distribution along the *x*-axis for (a) Au NPs/$ZnIn_2S_4$/TiO_2 and (b) Ag NPs/$ZnIn_2S_4$/TiO_2. c,d) UV–vis absorption spectra and photocatalytic CO_2 reduction performance of TiO_2, $ZnIn_2S_4$/TiO_2, Ag NPs/$ZnIn_2S_4$/TiO_2, Au NPs/$ZnIn_2S_4$/TiO_2 and $ZnIn_2S_4$. e) Simulated EM field distribution of Au/XS_2/Au antenna–reactor hybrids. f) Scheme of underlying mechanisms in the Au/XS_2/Au antenna–reactor hybrids for photocatalysis. g,h) H_2 evolution performance of different photocatalysts. a-d) Reproduced with permission.[111] Copyright 2015, Wiley-VCH. e-h) Reproduced with permission.[82] Copyright 2018, RSC.

Similarly, in the Au/XS_2/Au antenna–reactor hybrids, charge transfer process dominates in photocatalytic H_2 evolution for Au/ReS_2/Au, while strong coupled EM field contribute more to the photocatalytic activity in Au/MoS_2/Au via PIRET, as shown in Figure 13f.[82] Compared with Au/XS_2 hybrids, Au/XS_2/Au hybrids showed a photocatalytic H_2 generation rate with 2-fold and 1.5-fold enhancement for MoS_2 and ReS_2, respectively. Semiconductor spacers such as ultrathin MoS_2 or ReS_2 layer possess high carrier density and mobility. As a result, hot spots of coupled metal nanostructures and catalytic active sites of semiconductor spacers can jointly bring about enhanced solar-driven reactions.[141]

5. Conclusions and Perspectives

In summary, we have discussed the fundamentals of plasmonic coupling effect and the application of various plasmonic coupling architectures in photocatalysis. Comparing with the LSPR of isolated metal nanoparticles, the plasmonic coupling in coupled metal nanostructures exhibits unique advantages including remarkably enhanced local EM field, expanded hot spot area, and tunable plasmonic bands in a wide spectral range, which provide versatile opportunities in plasmonic photocatalysis with enhanced performance. However, some challenges still exist in the rational design of plasmonic coupling configurations to be effectively applied in photocatalytic reactions. In this section, we will highlight the typical challenging issues in the synthetic approaches of coupled metal nanostructures, and strive to provide a prospective view of further development of plasmonic coupling architectures for efficient photocatalysis. We hope the proposed futuristic picture may inspire new thought about plasmonic coupling and motivate researchers in sustainable solar-to-chemical transformation.

From the viewpoint of formation of coupled metal nanostructures, the most critical challenge is controlling the spacing between individual nano-components and their relative positions. Previous studies have demonstrated that the plasmonic coupling effect is closely correlated with the interparticle distance, which determines the local EM field intensity and the coupled LSPR frequencies. When multiple metal NPs are integrated in the coupled architecture, the relative position between the NPs become significant because it influences the directions of interparticle dipolar interactions. This issue is particularly important if anisotropic metal nanostructures are involved, and their orientation acts as an additional factor to impact plasmonic coupling.

Self-assembly is a convenient approach to obtained different configurations (e.g. dimer, oligomers, nanochains, and 2D superlattice) of couple metal nanoparticles through assistance from different external sources, such as surface ligands, polymers, templates and liquid interface. While the great challenge is how to effectively utilize the photo-activities of coupled

metal nanostructures for chemical reactions. Directly using the self-assembled metal nanostructures for plasmon-driven reactions is not efficient because the surface ligands, which are required for the assembly process, would inhibit adsorption of reactant molecules and reduce the lifetime of photogenerated charges on the metal surface. Alternatively, one may consider transfer of the pre-formed coupled metal NPs to the surface or matrix of a semiconductor photocatalyst, nevertheless, the risk is loss or change of spacing between metal NPs during the transfer process.

The more feasible way is building plasmonic coupling architectures on the structure of semiconductor photocatalysts. Although it is tough to precisely control the spacing of metal NPs in the matrix or on the surface of semiconductors, this issue may not be critically important in terms of applications towards maximal reaction efficiency. Smaller interparticle distance certainly could supply stronger local EM field between metal NPs, however, the effective volume of impacting nearby semiconductors by plasmonic coupling would be smaller. Thus, we will need to attain an optimal balance between the strongly enhanced EM field and the large hot spot area.

Considering the structural configurations, forming core–shell nanostructures is a promising strategy to achieve desirable plasmonic coupling effect. One way is confining coupled metal NPs in the semiconductor matrix with controllable interparticle distance. Orientation-dependent and configuration-dependent plasmonic coupling effect could also be established through delicate design and built-in fabrication in these core–shell nanostructures. The most ideal configuration is embedding the 3D oligomer core of metal NPs in a thin shell of mesoporous semiconductor photocatalyst. The strong three-dimensional interparticle plasmonic coupling will be able to impact large volume of semiconductors, which allow for enhancing the photocatalytic activities through different energy and/or charge transfer processes (e.g. PIRET, DET, etc.)

Another easily accessible approach is using semiconductor photocatalysts as the spacers to create metal–semiconductor–metal core–shell structure to achieve multi-interfacial plasmonic coupling, which has been demonstrated by some research groups.[78,82] This strategy can supply large hot spot volume covering the entire semiconductor spacer through strong plasmon coupling between the metal NP core and decorated metal NPs on the semiconductor shell. The wide choices of semiconductor spacers and metal NP compositions provide broad future opportunities on desirable combination designs to achieve high efficiencies in different photocatalytic reactions.

Moreover, the metal–semiconductor–metal core–shell configuration allows for construction of antenna−reactor systems with semiconductor spacers. The antenna is responsible for harvesting light and concentrating the photon energy at the near surface, and could be composed by different plasmonic structures, such as isolated metal nanoparticles, nanowires, patterned metal nanostructures, and coupled metal nanostructures. While the reactor part could be light-inactive metal nanoparticles that have specific catalytic activities for certain reactions. The plasmonic coupling between antenna and reactor can create strong EM field on the reactor metal surface as hot spots, where the surface catalytic reactions might be greatly enhanced. This is a unique feature allowing us to use light to initialize chemical reactions, which normally require high temperature to overcome energy barrier, on a light-inactive metal surface at room temperature with assistance of plasmonic coupling excitation.

Overall, rational design and precise modulation of plasmonic coupling architectures will provide optimal enhancement on the optical performance, charge kinetics and photocatalytic activities. The unique advantages of plasmonic coupling ensure its promising future applications particularly for photocatalysis and solar energy conversion. We hope that this review of recent development of plasmonic coupling architectures will bring new impetuses in

this field of plasmonic photocatalysis, which will play more important roles to meet the challenges in energy, environment, and sustainability.

Acknowledgements

The authors thank the support from the Ministry of Education, Singapore, under AcRF-Tier2 (MOE2018-T2-1-017) and AcRF-Tier1 (MOE2019-T1-002-012, RG102/19).

Conflict of Interest

The authors declare no conflict of interest.

Received: ((will be filled in by the editorial staff))
Revised: ((will be filled in by the editorial staff))
Published online: ((will be filled in by the editorial staff))

References

[1] D. M. Schultz, T. P. Yoon, *Science* **2014**, *343*, 1239176.

[2] S. Chen, T. Takata, K. Domen, *Nat. Rev. Mater.* **2017**, *2*, 17050.

[3] T. Yao, X. An, H. Han, J. Q. Chen, C. Li, *Adv. Energy Mater.* **2018**, *8*, 1800210.

[4] Z. Zhang, C. Zhang, H. Zheng, H. Xu, *Acc. Chem. Res.* **2019**, *52*, 2506.

[5] L. Mascaretti, A. Dutta, S. Kment, V. M. Shalaev, A. Boltasseva, R. Zboril, A. Naldoni, *Adv. Mater.* **2019**, *31*, 1805513.

[6] P. Zhang, T. Wang, J. Gong, *Adv. Mater.* **2015**, *27*, 5328.

[7] Y.-P. Yuan, L.-W. Ruan, J. Barber, S. C. J. Loo, C. Xue, *Energy Environ. Sci.* **2014**, *7*, 3934.

[8] U. Aslam, V. G. Rao, S. Chavez, S. Linic, *Nat. Catal.* **2018**, *1*, 656.

[9] S. Linic, P. Christopher, D. B. Ingram, *Nat. Mater.* **2011**, *10*, 911.

[10] J. G. Smith, J. A. Faucheaux, P. K. Jain, *Nano Today* **2015**, *10*, 67.

[11] Y. Xiong, R. Long, D. Liu, X. Zhong, C. Wang, Z.-Y. Li, Y. Xie, *Nanoscale* **2012**, *4*,

4416.

[12] D. Liu, D. Yang, Y. Gao, J. Ma, R. Long, C. Wang, Y. Xiong, *Angew. Chem., Int. Ed.* **2016**, *55*, 4577.

[13] P. Huang, J. Lin, W. Li, P. Rong, Z. Wang, S. Wang, X. Wang, X. Sun, M. Aronova, G. Niu, R. D. Leapman, Z. Nie, X. Chen, *Angew. Chem., Int. Ed.* **2013**, *52*, 13958.

[14] C. D. Geddes, *Reviews in Plasmonics 2017*, Springer, Cham, Switzerland **2019**.

[15] S. G. Park, C. Mun, M. Lee, T. Y. Jeon, H. S. Shim, Y. J. Lee, J. D. Kwon, C. S. Kim, D. H. Kim, *Adv. Mater.* **2015**, *27*, 4290.

[16] S. A. Maier, *Plasmonics: Fundamentals and Applications*, Springer, New York, USA **2007**.

[17] G. Baffou, R. Quidant, *Chem. Soc. Rev.* **2014**, *43*, 3898.

[18] K. L. Kelly, E. Coronado, L. L. Zhao, G. C. Schatz, *J. Phys. Chem. B* **2003**, *107*, 668.

[19] X. C. Ma, Y. Dai, L. Yu, B. B. Huang, *Light Sci. Appl.* **2016**, *5*, e16017.

[20] S.-W. Cao, Z. Yin, J. Barber, F. Y. Boey, S. C. Loo, C. Xue, *ACS Appl. Mater. Interfaces* **2012**, *4*, 418.

[21] S.-W. Cao, J. Fang, M. M. Shahjamali, F. Y. C. Boey, J. Barber, S. C. J. Loo, C. Xue, *RSC Adv.* **2012**, *2*, 5513.

[22] U. Aslam, S. Chavez, S. Linic, *Nat. Nanotechnol.* **2017**, *12*, 1000.

[23] Z. Zheng, T. Tachikawa, T. Majima, *J. Am. Chem. Soc.* **2014**, *136*, 6870.

[24] K. H. W. Ho, A. Shang, F. Shi, T. W. Lo, P. H. Yeung, Y. S. Yu, X. Zhang, K.-y. Wong, D. Y. Lei, *Adv. Funct. Mater.* **2018**, *28*, 1800383.

[25] Z. Zhang, A. Li, S. W. Cao, M. Bosman, S. Li, C. Xue, *Nanoscale* **2014**, *6*, 5217.

[26] Z. Zhang, Z. Wang, S.-W. Cao, C. Xue, *J. Phys. Chem. C* **2013**, *117*, 25939.

[27] A. Gelle, T. Jin, L. de la Garza, G. D. Price, L. V. Besteiro, A. Moores, *Chem. Rev.* **2020**, *120*, 986.

[28] R. Long, Y. Li, L. Song, Y. Xiong, *Small* **2015**, *11*, 3873.

[29] W. Jiang, S. Bai, L. Wang, X. Wang, L. Yang, Y. Li, D. Liu, X. Wang, Z. Li, J. Jiang, Y. Xiong, *Small* **2016**, *12*, 1640.

[30] N. J. Greybush, I. Liberal, L. Malassis, J. M. Kikkawa, N. Engheta, C. B. Murray, C. R. Kagan, *ACS Nano* **2017**, *11*, 2917.

[31] W. Rechberger, A. Hohenau, A. Leitner, J. R. Krenn, B. Lamprecht, F. R. Aussenegg, *Opt. Commun.* **2003**, *220*, 137.

[32] P. K. Jain, M. A. El-Sayed, *Chem. Phys. Lett.* **2010**, *487*, 153.

[33] S. J. Barrow, A. M. Funston, D. E. Gomez, T. J. Davis, P. Mulvaney, *Nano Lett.* **2011**, *11*, 4180.

[34] A. Klinkova, R. M. Choueiri, E. Kumacheva, *Chem. Soc. Rev.* **2014**, *43*, 3976.

[35] D. Paria, K. Roy, H. J. Singh, S. Kumar, S. Raghavan, A. Ghosh, A. Ghosh, *Adv. Mater.* **2015**, *27*, 1751.

[36] T.-H. Yang, Y.-W. Harn, M.-Y. Pan, L.-D. Huang, M.-C. Chen, B.-Y. Li, P.-H. Liu, P.-Y. Chen, C.-C. Lin, P.-K. Wei, L.-J. Chen, J.-M. Wu, *Appl. Catal. B* **2016**, *181*, 612.

[37] K. Li, N. J. Hogan, M. J. Kale, N. J. Halas, P. Nordlander, P. Christopher, *Nano Lett.* **2017**, *17*, 3710.

[38] A. G. da Silva, T. S. Rodrigues, V. G. Correia, T. V. Alves, R. S. Alves, R. A. Ando, F. R. Ornellas, J. Wang, L. H. Andrade, P. H. Camargo, *Angew. Chem., Int. Ed.* **2016**, *55*, 7111.

[39] P. K. Jain, W. Huang, M. A. El-Sayed, *Nano Lett.* **2007**, *7*, 2080.

[40] M. Hentschel, M. Saliba, R. Vogelgesang, H. Giessen, A. P. Alivisatos, N. Liu, *Nano Lett.* **2010**, *10*, 2721.

[41] Y. C. Tsao, S. Rej, C. Y. Chiu, M. H. Huang, *J. Am. Chem. Soc.* **2014**, *136*, 396.

[42] C. Hanske, M. Tebbe, C. Kuttner, V. Bieber, V. V. Tsukruk, M. Chanana, T. A. Konig, A. Fery, *Nano Lett.* **2014**, *14*, 6863.

[43] P. K. Jain, S. Eustis, M. A. El-Sayed, *J. Phys. Chem. B* **2006**, *110*, 18243.

[44] C. Tabor, D. Van Haute, M. A. El-Sayed, *ACS Nano* **2009**, *3*, 3670.

[45] N. Hooshmand, J. A. Bordley, M. A. El-Sayed, *J. Phys. Chem. C* **2016**, *120*, 4564.

[46] X. Zhang, Y. L. Chen, R. S. Liu, D. P. Tsai, *Rep. Prog. Phys.* **2013**, *76*, 046401.

[47] J. B. Lee, S. Choi, J. Kim, Y. S. Nam, *Nano Today* **2017**, *16*, 61.

[48] E. Hutter, J. H. Fendler, *Adv. Mater.* **2004**, *16*, 1685.

[49] Y. Xia, N. J. Halas, *MRS Bull.* **2011**, *30*, 338.

[50] P. K. Jain, M. A. El-Sayed, *Nano Lett.* **2008**, *8*, 4347.

[51] E. R. Encina, E. A. Coronado, *J. Phys. Chem. C* **2010**, *114*, 3918.

[52] N. J. Halas, S. Lal, W. S. Chang, S. Link, P. Nordlander, *Chem. Rev.* **2011**, *111*, 3913.

[53] S. Gwo, H. Y. Chen, M. H. Lin, L. Sun, X. Li, *Chem. Soc. Rev.* **2016**, *45*, 5672.

[54] V. L. Y. Loke, G. M. Huda, E. U. Donev, V. Schmidt, J. T. Hastings, M. P. Mengüç, T. Wriedt, *Appl. Catal. B* **2013**, *115*, 237.

[55] E. Hao, G. C. Schatz, *J. Chem. Phys.* **2004**, *120*, 357.

[56] J. A. Fan, C. Wu, K. Bao, J. Bao, R. Bardhan, N. J. Halas, V. N. Manoharan, P. Nordlander, G. Shvets, F. Capasso, *Science* **2010**, *328*, 1135.

[57] J. Li, S. K. Cushing, P. Zheng, F. Meng, D. Chu, N. Wu, *Nat. Commun.* **2013**, *4*, 2651.

[58] V. Flauraud, G. D. Bernasconi, J. Butet, D. T. L. Alexander, O. J. F. Martin, J. Brugger, *ACS Nano* **2017**, *11*, 3485.

[59] D. Lee, S. Yoon, *J. Phys. Chem. C* **2015**, *119*, 7873.

[60] A. Tao, P. Sinsermsuksakul, P. Yang, *Nat. Nanotechnol.* **2007**, *2*, 435.

[61] D. O. Sigle, L. Zhang, S. Ithurria, B. Dubertret, J. J. Baumberg, *J. Phys. Chem. Lett.* **2015**, *6*, 1099.

[62] M. Dhiman, A. Maity, A. Das, R. Belgamwar, B. Chalke, Y. Lee, K. Sim, J. M. Nam, V. Polshettiwar, *Chem. Sci.* **2019**, *10*, 6594.

[63] Q. Sun, H. Yu, K. Ueno, S. Zu, Y. Matsuo, H. Misawa, *Opto-Electron. Adv.* **2019**, *2*, 18003001.

[64] S. S. Acimovic, M. P. Kreuzer, M. U. Gonzalez, R. Quidant, *ACS Nano* **2009**, *3*, 1231.

[65] X. Yu, D. Y. Lei, F. Amin, R. Hartmann, G. P. Acuna, A. Guerrero-Martínez, S. A. Maier, P. Tinnefeld, S. Carregal-Romero, W. J. Parak, *Nano Today* **2013**, *8*, 480.

[66] M. Vadai, D. K. Angell, F. Hayee, K. Sytwu, J. A. Dionne, *Nat. Commun.* **2018**, *9*, 4658.

[67] C. Tabor, R. Murali, M. Mahmoud, M. A. El-Sayed, *J. Phys. Chem. A* **2009**, *113*, 1946.

[68] J. A. Bordley, N. Hooshmand, M. A. El-Sayed, *Nano Lett.* **2015**, *15*, 3391.

[69] S. Sheikholeslami, Y. W. Jun, P. K. Jain, A. P. Alivisatos, *Nano Lett.* **2010**, *10*, 2655.

[70] M. B. Ross, C. A. Mirkin, G. C. Schatz, *J. Phys. Chem. C* **2016**, *120*, 816.

[71] A. W. Clark, D. G. Thompson, D. Graham, J. M. Cooper, *Adv. Mater.* **2014**, *26*, 4286.

[72] A. S. Urban, X. Shen, Y. Wang, N. Large, H. Wang, M. W. Knight, P. Nordlander, H. Chen, N. J. Halas, *Nano Lett.* **2013**, *13*, 4399.

[73] A. M. Funston, C. Novo, T. J. Davis, P. Mulvaney, *Nano Lett.* **2009**, *9*, 1651.

[74] L. Shao, C. Fang, H. Chen, Y. C. Man, J. Wang, H. Q. Lin, *Nano Lett.* **2012**, *12*, 1424.

[75] E. Prodan, C. Radloff, N. J. Halas, P. Nordlander, *Science* **2003**, *302*, 419.

[76] N. Hooshmand, M. A. El-Sayed, *Proc. Natl. Acad. Sci. U.S.A.* **2019**, *116*, 19299.

[77] P. K. Jain, M. A. El-Sayed, *Nano Lett.* **2007**, *7*, 2854.

[78] L. Ma, Y. L. Chen, D. J. Yang, H. X. Li, S. J. Ding, L. Xiong, P. L. Qin, X. B. Chen, *Nanoscale* **2020**, *12*, 4383.

[79] M. Lin, G. H. Kim, J. H. Kim, J. W. Oh, J. M. Nam, *J. Am. Chem. Soc.* **2017**, *139*, 10180.

[80] H. Zhang, C. Guan, N. Song, Y. Zhang, H. Liu, J. Fang, *Phys. Chem. Chem. Phys.* **2018**, *20*, 3571.

[81] D. Manchon, J. Lerme, T. Zhang, A. Mosset, C. Jamois, C. Bonnet, J. M. Rye, A. Belarouci, M. Broyer, M. Pellarin, E. Cottancin, *Nanoscale* **2015**, *7*, 1181.

[82] K. Chen, S. J. Ding, Z. J. Luo, G. M. Pan, J. H. Wang, J. Liu, L. Zhou, Q. Q. Wang, *Nanoscale* **2018**, *10*, 4130.

[83] B. Yu, J. I. Tracey, Z. Cheng, M. Vacha, D. M. O'Carroll, *Phys. Chem. Chem. Phys.* **2018**, *20*, 11749.

[84] D. E. Gómez, T. J. Davis, A. M. Funston, *J. Mater. Chem. C* **2014**, *2*, 3077.

[85] W. Q. Li, G. Wang, X. N. Zhang, H. P. Geng, J. L. Shen, L. S. Wang, J. Zhao, L. F. Xu, L. J. Zhang, Y. Q. Wu, R. Z. Tai, G. Chen, *Nanoscale* **2015**, *7*, 15487.

[86] B. B. Rajeeva, L. Lin, Y. Zheng, *Nano Res.* **2018**, *11*, 4423.

[87] F. Qin, L. Ding, L. Zhang, F. Monticone, C. C. Chum, J. Deng, S. Mei, Y. Li, J. Teng, M. Hong, S. Zhang, A. Alu, C. W. Qiu, *Sci. Adv.* **2016**, *2*, e1501168.

[88] C. Zhang, H. Zhao, L. Zhou, A. E. Schlather, L. Dong, M. J. McClain, D. F. Swearer, P. Nordlander, N. J. Halas, *Nano Lett.* **2016**, *16*, 6677.

[89] J. K. Kim, X. Shi, M. J. Jeong, J. E. Park, H. S. Han, S. H. Kim, Y. Guo, T. F. Heinz, S. Fan, C.-L. Lee, J. H. Park, X. Zheng, *Adv. Energy Mater.* **2018**, *8*, 1701765.

[90] T. R. Jensen, M. D. Malinsky, C. L. Haynes, R. P. Van Duyne, *J. Phys. Chem. B* **2000**, *104*, 10549.

[91] P. Zheng, S. Kasani, N. Wu, *Nanoscale Horiz.* **2019**, *4*, 516.

[92] X. Wang, R. Long, D. Liu, D. Yang, C. Wang, Y. Xiong, *Nano Energy* **2016**, *24*, 87.

[93] A. Zhu, R. Gao, X. Zhao, F. Zhang, X. Zhang, J. Yang, Y. Zhang, L. Chen, Y. Wang, *Nanoscale* **2019**, *11*, 6576.

[94] B. Shen, V. Linko, K. Tapio, S. Pikker, T. Lemma, A. Gopinath, K. V. Gothelf, M. A. Kostiainen, J. J. Toppari, *Sci. Adv.* **2018**, *4*, eaap8978.

[95] J. Theiss, P. Pavaskar, P. M. Echternach, R. E. Muller, S. B. Cronin, *Nano Lett.* **2010**, *10*, 2749.

[96] X. Lu, M. Rycenga, S. E. Skrabalak, B. Wiley, Y. Xia, *Annu. Rev. Phys. Chem.* **2009**, *60*,

167.

[97] S. Lee, J. Kim, H. Yang, E. Cortes, S. Kang, S. W. Han, *Angew. Chem., Int. Ed.* **2019**, *58*, 15890.

[98] S. Lee, J. W. Hong, S. U. Lee, Y. W. Lee, S. W. Han, *Chem. Commun.* **2015**, *51*, 8793.

[99] M. A. Mahmoud, M. A. El-Sayed, *J. Am. Chem. Soc.* **2010**, *132*, 12704.

[100] J. Zhu, J.-K. Chen, J.-J. Li, J.-W. Zhao, *Appl. Phys. A* **2019**, *125*, 62.

[101] X. Li, S. Guo, C. Kan, J. Zhu, T. Tong, S. Ke, W. C. H. Choy, B. Wei, *Nano Energy* **2016**, *30*, 549.

[102] S. Kamimura, S. Yamashita, S. Abe, T. Tsubota, T. Ohno, *Appl. Catal. B* **2017**, *211*, 11.

[103] M. Mayer, A. M. Steiner, F. Roder, P. Formanek, T. A. F. Konig, A. Fery, *Angew. Chem., Int. Ed.* **2017**, *56*, 15866.

[104] S. Lee, Y. Wy, Y. W. Lee, K. Ham, S. W. Han, *Small* **2017**, *13*, 1701633.

[105] J. Kim, S. Yoo, J. M. Kim, S. Choi, J. Kim, S. J. Park, D. Park, J. M. Nam, S. Park, *Nano Lett.* **2020**, *20*, 4362.

[106] J. H. Yoon, J. Lim, S. Yoon, *ACS Nano* **2012**, *6*, 7199.

[107] N. Gandra, A. Abbas, L. Tian, S. Singamaneni, *Nano Lett.* **2012**, *12*, 2645.

[108] J. W. Oh, D. K. Lim, G. H. Kim, Y. D. Suh, J. M. Nam, *J. Am. Chem. Soc.* **2014**, *136*, 14052.

[109] J. Li, Y. Long, Y. Liu, L. Zhang, Q. Wang, X. Wang, S. Song, H. Zhang, *Angew. Chem., Int. Ed.* **2020**, *59*, 1103.

[110] A. Kumar, N. Kumari, S. Dubbu, S. Kumar, T. Kwon, J. H. Koo, J. Lim, I. Kim, Y. K. Cho, J. Rho, I. S. Lee, *Angew. Chem., Int. Ed.* **2020**, *59*, 9460.

[111] Z. Zhang, Y. Huang, K. Liu, L. Guo, Q. Yuan, B. Dong, *Adv. Mater.* **2015**, *27*, 5906.

[112] U. Cataldi, R. Caputo, Y. Kurylyak, G. Klein, M. Chekini, C. Umeton, T. Bürgi, *J. Mater. Chem. C* **2014**, *2*, 7927.

[113] D. F. Swearer, H. Zhao, L. Zhou, C. Zhang, H. Robatjazi, J. M. Martirez, C. M. Krauter, S. Yazdi, M. J. McClain, E. Ringe, E. A. Carter, P. Nordlander, N. J. Halas, *Proc. Natl. Acad. Sci. U.S.A.* **2016**, *113*, 8916.

[114] J. Zhang, Y. Sun, R. Feng, W. Liang, Z. Liang, W. Guo, I. Abdulhalim, J. Qu, C. W. Qiu, L. Jiang, *Nanoscale* **2019**, *11*, 23058.

[115] S. J. Barrow, A. M. Funston, X. Wei, P. Mulvaney, *Nano Today* **2013**, *8*, 138.

[116] D. J. Park, C. Zhang, J. C. Ku, Y. Zhou, G. C. Schatz, C. A. Mirkin, *Proc. Natl. Acad. Sci. U.S.A.* **2015**, *112*, 977.

[117] D. Liu, F. Zhou, C. Li, T. Zhang, H. Zhang, W. Cai, Y. Li, *Angew. Chem., Int. Ed.* **2015**, *54*, 9596.

[118] V. Gupta, P. T. Probst, F. R. Gossler, A. M. Steiner, J. Schubert, Y. Brasse, T. A. F. Konig, A. Fery, *ACS Appl. Mater. Interfaces* **2019**, *11*, 28189.

[119] K. Volk, J. P. Fitzgerald, M. Retsch, M. Karg, *Adv. Mater.* **2015**, *27*, 7332.

[120] Y. H. Lee, W. Shi, H. K. Lee, R. Jiang, I. Y. Phang, Y. Cui, L. Isa, Y. Yang, J. Wang, S. Li, X. Y. Ling, *Nat. Commun.* **2015**, *6*, 6990.

[121] L. Velleman, D. Sikdar, V. A. Turek, A. R. Kucernak, S. J. Roser, A. A. Kornyshev, J. B. Edel, *Nanoscale* **2016**, *8*, 19229.

[122] M. E. J. Hummel, C. Stelling, B. A. F. Kopera, F. A. Nutz, M. Karg, M. Retsch, S. Forster, *Langmuir* **2019**, *35*, 973.

[123] M. Mayer, M. Tebbe, C. Kuttner, M. J. Schnepf, T. A. Konig, A. Fery, *Faraday Discuss.* **2016**, *191*, 159.

[124] D. Liu, J. Ma, R. Long, C. Gao, Y. Xiong, *Nano Today* **2017**, *17*, 96.

[125] S. K. Cushing, J. Li, F. Meng, T. R. Senty, S. Suri, M. Zhi, M. Li, A. D. Bristow, N. Wu, *J. Am. Chem. Soc.* **2012**, *134*, 15033.

[126] H. Huang, L. Zhang, Z. Lv, R. Long, C. Zhang, Y. Lin, K. Wei, C. Wang, L. Chen, Z.-Y.

Li, Q. Zhang, Y. Luo, Y. Xiong, *J. Am. Chem. Soc.* **2016**, *138*, 6822.

[127] J. Fang, S.-W. Cao, Z. Wang, M. M. Shahjamali, S. C. J. Loo, J. Barber, C. Xue, *Int. J. Hydrog. Energy* **2012**, *37*, 17853.

[128] L. Zhou, J. M. P. Martirez, J. Finzel, C. Zhang, D. F. Swearer, S. Tian, H. Robatjazi, M. Lou, L. Dong, L. Henderson, P. Christopher, E. A. Carter, P. Nordlander, N. J. Halas, *Nat. Energy* **2020**, *5*, 61.

[129] H. Song, X. Meng, T. D. Dao, W. Zhou, H. Liu, L. Shi, H. Zhang, T. Nagao, T. Kako, J. Ye, *ACS Appl. Mater. Interfaces* **2018**, *10*, 408.

[130] E. Peiris, S. Sarina, E. R. Waclawik, G. A. Ayoko, P. Han, J. Jia, H. Y. Zhu, *Angew. Chem., Int. Ed.* **2019**, *58*, 12032.

[131] S. Li, P. Miao, Y. Zhang, J. Wu, B. Zhang, Y. Du, X. Han, J. Sun, P. Xu, *Adv. Mater.* **2020**, 2000086.

[132] J. Zhang, X. Jin, P. I. Morales-Guzman, X. Yu, H. Liu, H. Zhang, L. Razzari, J. P. Claverie, *ACS Nano* **2016**, *10*, 4496.

[133] C. Climent, J. Galego, F. J. Garcia-Vidal, J. Feist, *Angew. Chem., Int. Ed.* **2019**, *58*, 8698.

[134] P. Muhlschlegel, H. J. Eisler, O. J. Martin, B. Hecht, D. W. Pohl, *Science* **2005**, *308*, 1607.

[135] Z. Yin, Y. Wang, C. Song, L. Zheng, N. Ma, X. Liu, S. Li, L. Lin, M. Li, Y. Xu, W. Li, G. Hu, Z. Fang, D. Ma, *J. Am. Chem. Soc.* **2018**, *140*, 864.

[136] N. Zou, G. Chen, X. Mao, H. Shen, E. Choudhary, X. Zhou, P. Chen, *ACS Nano* **2018**, *12*, 5570.

[137] Y. Negrín-Montecelo, M. Comesaña-Hermo, X.-T. Kong, B. Rodríguez-González, Z. Wang, M. Pérez-Lorenzo, A. O. Govorov, M. A. Correa-Duarte, *ChemCatChem* **2018**, *10*, 1561.

[138] W. Zhao, B. Dai, F. Zhu, X. Tu, J. Xu, L. Zhang, S. Li, D. Y. C. Leung, S. Cheng, *Appl. Catal. B* **2018**, *229*, 171.

[139] M. Wang, J. Zhang, P. Wang, C. Li, X. Xu, Y. Jin, *Nano Res.* **2018**, *11*, 3854.

[140] Y. Liu, Z. Zhang, Y. Fang, B. Liu, J. Huang, F. Miao, Y. Bao, B. Dong, *Appl. Catal. B* **2019**, *252*, 164.

[141] H. Wang, T. You, W. Shi, J. Li, L. Guo, *J. Phys. Chem. C* **2012**, *116*, 6490.

[142] A. E. Schlather, A. Manjavacas, A. Lauchner, V. S. Marangoni, C. J. DeSantis, P. Nordlander, N. J. Halas, *J. Phys. Chem. Lett.* **2017**, *8*, 2060.

[143] Y. Liu, F. Chen, Q. Wang, J. Wang, J. Wang, *Appl. Catal. B* **2018**, *224*, 940.

[144] Y. M. Choi, B. W. Lee, M. S. Jung, H. S. Han, S. H. Kim, K. Chen, D. H. Kim, T. F. Heinz, S. Fan, J. Lee, G. R. Yi, J. K. Kim, J. H. Park, *Adv. Energy Mater.* **2020**, *10*, 2000570.

[145] H. Shan, Y. Yu, X. Wang, Y. Luo, S. Zu, B. Du, T. Han, B. Li, Y. Li, J. Wu, F. Lin, K. Shi, B. K. Tay, Z. Liu, X. Zhu, Z. Fang, *Light Sci. Appl.* **2019**, *8*, 9.

Biographies

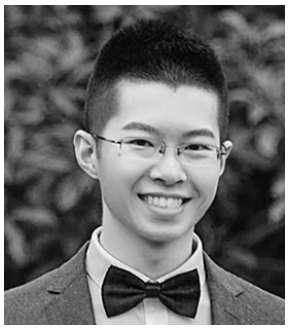

Dong Liu obtained his B.Sc. degree (2012, Special Class for the Gifted Young) and Ph.D. degree (2017) from the University of Science and Technology of China. In 2019, he joined Prof. Xue's group as a research fellow at the School of Materials Science and Engineering, Nanyang Technological University, Singapore. His research interests focus on developing low-dimensional nanostructures for solar-driven production of fuels and valuable chemicals.

Can Xue is currently a tenured associate professor in the School of Materials Science and Engineering, Nanyang Technological University, Singapore. He received his B.Sc. degree (Special Class for the Gifted Young) in 2002 from University of Science and Technology of China and his Ph.D degree (2007) at Northwestern University (IL, USA). His major research activities are devoted to exploring photocatalytic applications of plasmonic metal nanostructures and developing novel metal-semiconductor hybrid nanomaterials for solar-driven water splitting and CO_2 reduction.

Excitation of plasmonic coupling architectures induces extremely strong local electromagnetic field that can significantly impact nearby semiconductors through plasmon-driven charge/energy transfer to enhance the photocatalytic activities. Recent advances in the development of plasmonic coupling architectures and different strategies of integration with semiconductor photocatalysts are reviewed. Remaining challenges and future prospects of plasmonic coupling for sustainable solar-driven reactions are also discussed.

Dr. D. Liu, Prof. C. Xue*

Plasmonic Coupling Architectures for Enhanced Photocatalysis